PORTLAND PRESS

Research Article

1-Deoxy-D-xylulose 5-phosphate reductoisomerase as target for anti *Toxoplasma gondii* agents: crystal structure, biochemical characterization and biological evaluation of inhibitors

Flaminia Mazzone[1,2], Astrid Hoeppner[3], Jens Reiners[3], Christoph G.W. Gertzen[3,4], Violetta Applegate[3], Mona A. Abdullaziz[4,5], Julia Gottstein[6], Daniel Degrandi[1,2], Martina Wesemann[6], Thomas Kurz[4,*], Sander H.J. Smits[3,6*] and Klaus Pfeffer[1,2*]

[1]Institute of Medical Microbiology and Hospital Hygiene, Heinrich Heine University, Düsseldorf, Germany; [2]University Hospital Düsseldorf, Düsseldorf, Germany; [3]Center for Structural Studies, Heinrich Heine University, Düsseldorf, Germany; [4]Institute of Pharmaceutical and Medicinal Chemistry, Heinrich Heine University, Düsseldorf, Germany; [5]National Research Centre (NRC), Dokki, Cairo, Egypt; [6]Institute of Biochemistry, Heinrich Heine University, Düsseldorf, Germany

Correspondence: Klaus Pfeffer (klaus.pfeffer@hhu.de) or Sander H.J. Smits (sander.smits@hhu.de) or Flaminia Mazzone (flaminia.mazzone@hhu.de)

OPEN ACCESS

Toxoplasma gondii is a widely distributed apicomplexan parasite causing toxoplasmosis, a critical health issue for immunocompromised individuals and for congenitally infected foetuses. Current treatment options are limited in number and associated with severe side effects. Thus, novel anti-toxoplasma agents need to be identified and developed. 1-Deoxy-D-xylulose 5-phosphate reductoisomerase (DXR) is considered the rate-limiting enzyme in the non-mevalonate pathway for the biosynthesis of the isoprenoid precursors isopentenyl pyrophosphate and dimethylallyl pyrophosphate in the parasite, and has been previously investigated for its key role as a novel drug target in some species, encompassing *Plasmodia*, *Mycobacteria* and *Escherichia coli*. In this study, we present the first crystal structure of *T. gondii* DXR (*Tg*DXR) in a tertiary complex with the inhibitor fosmidomycin and the cofactor NADPH in dimeric conformation at 2.5 Å resolution revealing the inhibitor binding mode. In addition, we biologically characterize reverse α-phenyl-β-thia and β-oxa fosmidomycin analogues and show that some derivatives are strong inhibitors of *Tg*DXR which also, in contrast with fosmidomycin, inhibit the growth of *T. gondii in vitro*. Here, ((3,4-dichlorophenyl)((2-(hydroxy(methyl)amino)-2-oxoethyl)thio) methyl)phosphonic acid was identified as the most potent anti *T. gondii* compound. These findings will enable the future design and development of more potent anti-toxoplasma DXR inhibitors.

Introduction

Toxoplasma gondii, the causative agent of toxoplasmosis, is an obligate coccidian parasite member of the phylum Apicomplexa [1]. As all apicomplexans, *T. gondii* possesses a complex and heteroxenous life cycle alternating between sexual stages that occur exclusively in the intestinal epithelium of their definitive hosts (the family *Felidae*), and asexual stages that can take place virtually in any warm-blooded animal, including humans [2]. Therefore, the pathogenesis of *T. gondii* is profoundly influenced by the growth rate of its asexual stages [3]. It has reported that, in the United States, ~11% of the population aged 6 years and older have been infected with *T. gondii* [4]. In humans, the primary routes of infection are foodborne, caused by the consumption of raw or undercooked meat that contain tissue cysts (bradyzoites), or by ingestion of contaminated vegetables or water containing sporulated oocysts [5,6]. In healthy and immunocompetent individuals, toxoplasmosis typically

remains asymptomatic or manifests with flu-like symptoms, since the infection is efficiently controlled by a fully functional immune system [7,8]. On the other hand, the disease poses a significant concern in immuno-compromised individuals, often leading to the reactivation of latent infection with severe clinical manifestations, such as chorioretinitis, encephalitis, pneumonitis and sepsis-like symptoms [9]. Moreover, acute *T. gondii* infections of pregnant women are a relevant risk for the unborn, as maternal-to-fetal transmission of this infection can result in devastating ophthalmic and neurological consequences as well as fatalities for the fetus [10].

Currently, the gold-standard treatment for toxoplasmosis remains the antifolate combination of pyrimethamine and sulfadiazine (PYR-SLZ) [11]. Despite the advancements in target-based drug development in the post-genomic era, human toxoplasmosis lacks sufficient treatment options [12]. Furthermore, all the current available regimens suffer from several limitations and negative aspects that compromise patient compliance and overall effectiveness. These limitations include: a lack of specificity, that can cause severe and potentially fatal side effects; and the inability to effectively target bradyzoites, the dormant cyst-form of the parasite, responsible for the latency of the infection [13]. Therefore, novel, safer and more efficient therapeutic options are urgently needed.

Since its discovery, the apicoplast, a non-photosynthetic plastid organelle in the apicomplexan parasites has emerged has an attractive target for anti-infective drugs due to its absence in mammalian cells [14,15]. This plastid is responsible for essential metabolic pathways for the parasite such as fatty acid, haem, iron sulfur cluster, and synthesis of isoprenoids among others [16]. The 2-*C*-Methyl-D-erythritol 4-phosphate (MEP) pathway, also called non-mevalonate pathway, for the biosynthesis of isopentenyl pyrophosphate and dimethylallyl pyrophosphate (DMAPP), crucial metabolites for biosynthesis of isoprenoids and essential for the organism, has gathered high interest as a potential drug target (Figure 1). Its enzymes are highly conserved in plastid-bearing organisms and most gram-negative bacteria, and there are no mammalian orthologues, as humans and animals use the mevalonate pathway for the biosynthesis of isoprenoids [17–20].

The 1-Deoxy-D-xylulose 5-phosphate reductoisomerase (DXR, IspC, EC 1.1.1.267), the second and rate-limiting enzyme in the MEP pathway, catalyzes the isomerization and the reduction of 1-Deoxy-D-xylulose 5-phosphate (DXP) into MEP. The catalysis occurs with dependency of a metallic dication (Mg^{2+}) and NADPH
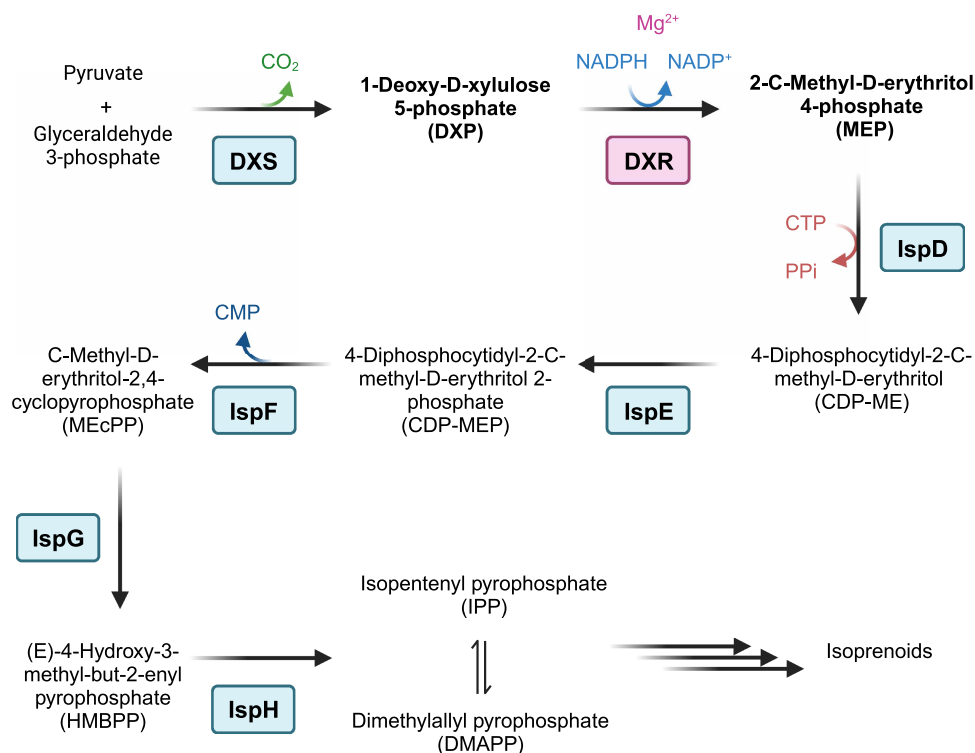

Figure 1. The MEP pathway for the biosynthesis of isoprenoids.
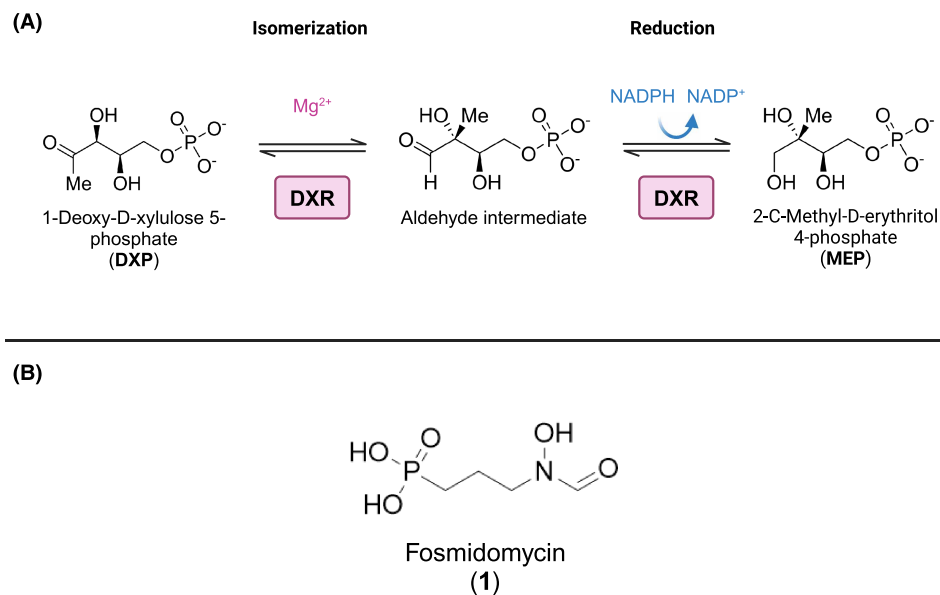Modified from Frank and Groll [86]. Created with BioRender.com.

Figure 2. Reaction catalyzed by 1-Deoxy-D-xylulose 5-phosphate reductoisomerase (DXR) and the inhibitor fosmidomycin.

(**A**) The DXR enzyme catalyzes the conversion of the substrate 1-Deoxy-D-xylulose 5-phosphate (DXP) into the product 2-C-Methyl-D-erythritol-4-phosphate (MEP). The catalysis occurs with dependency of a metallic dication (Mg^{2+}) and NADPH as cofactors. One of the proposed mechanisms consists of a two-step reaction: first, the retro-aldol/aldol isomerization of DXP with the formation of the aldehyde intermediate [87]; then, a NADPH-depend reduction of the intermediate to MEP [88]. Modified from Kuzuyama et al. [43]. (**B**) Chemical structure of the DXR inhibitor fosmidomycin. Created with BioRender.com.

as cofactors (Figure 2A). DXR enzymes have been extensively investigated and characterized for their key role in the pathway, and in particularly, for the development of novel antibacterial and antimalarial agents [21,22]. Moreover, several structural studies of this enzyme from different organism have been reported with high and medium resolution, such as the crystal structure of DXR from *Escherichia coli* [23], *Mycobacterium tuberculosis* [24], *Plasmodium falciparum* [25], but not from *T. gondii*.

Fosmidomycin (**1**) (Figure 2B), a natural product originally isolated from the bacteria *Streptomyces lavendulae* [26] was identified as a potent and specific inhibitor of the DXR enzymes from *E. coli* [27] and *P. falciparum* [28]. Unfortunately, this molecule faces several limitations as a clinical therapeutic related to its pharmacokinetics: short plasma half-life and rapid plasma clearance [29] as well as poor bioavailability due to the ionized nature of the phosphonate group of fosmidomycin at physiological pH [30]. Its polarity affects membrane permeability, except *E. coli* [31] that actively transports the compound. However, it is not effective in *M. tuberculosis* [32] and *T. gondii* [33] probably due to the lack of uptake systems.

Given the significance of DXR inhibitors and with the aim to identify improved inhibitors of *Tg*DXR, in the present study we successfully cloned, expressed, purified and biochemically characterized the recombinant *Tg*DXR. We report the X-ray structure of *Tg*DXR in a tertiary complex with the cofactor NADPH and the inhibitor fosmidomycin, further defined by small-angle X-ray scattering (SAXS) analysis. Moreover, we assessed the *in vitro* activity of previously described β-thia and β-oxa isosters of reverse hydroxamic acid analogues of fosmidomycin [34–36] against the activity of the recombinant *Tg*DXR enzyme and *T. gondii* proliferation. These findings could support the future design and development of novel anti-toxoplasma agents.

Results
Biochemical characterization
*Tg*DXR enzyme properties
We set out to functionally and structurally characterize the His$_{10}$-*Tg*DXR, which contains the catalytic domain. To achieve this, we constructed a plasmid, which contains the catalytic centre consisting of the NADPH

binding site as well as the substrate-binding site of the *Tg*DXR protein (amino acid 182–632) (Supplementary Figure S1). After expression, *Tg*DXR was purified to homogeneity as observed by a single symmetric peak on the size exclusion chromatography (SEC) profile and SDS–PAGE analysis (Figure 3). The purified *Tg*DXR was then evaluated for its enzymatic activity through a spectrophotometric assay measuring the oxidation of NADPH over time under various conditions. The optimum of its catalytic capacity was reached with 100 µM of DXP, 100 µM of NADPH, 4 mM of MgCl$_2$ and a pH of 7.5 at concentration of 100 nM of *Tg*DXR (Figure 3). The kinetic parameters of *Tg*DXR were also evaluated: the K_m value for DXP was determined to be 30.58 ± 6.33 µM, which is comparable with the *Tg*DXR K_m value obtained previously [37] and the reported DXR K_m values from other species, such as *Pf*DXR (67 µM) [38] and *Mt*DXR (47 µM) [39]; the K_m for NADPH was determined as 51.30 ± 11.84 µM (Figure 3). The V_{max} was shown to be 0.83 mmol/min/mg, comparable to *Pf*DXR (1.04 mmol/min/mg) [38].

Structural characterization of the *Tg*DXR catalytic domain

*Tg*DXR was crystallised in the presence of the known inhibitor fosmidomycin using the sitting drop method. The 3 µl drops consisted of 1.5 µl protein (7.5 mg/ml in 20 mM TRIS pH 7.5, 150 mM NaCl, 2% glycerol supplemented with 1 mM fosmidomycin, 4 mM MgCl$_2$ and 4 mM NADPH) mixed with crystallization buffer 1.5 µl 200 mM Na citrate tribasic, 27% PEG smear low, 150 mM HEPES pH 7.8. Crystallization was performed at 12°C and crystals appeared within a few days and grew to their final dimensions within two weeks. Before the crystals were flash-cooled in liquid nitrogen, the crystallization drops were overlaid with mineral oil and the crystals were dragged through it during crystal harvesting. A high-resolution dataset was collected and phased using the model of the DXR protein from *E. coli* (PDB entry: 1K5H) [40] revealing a dimer in the asymmetric unit.
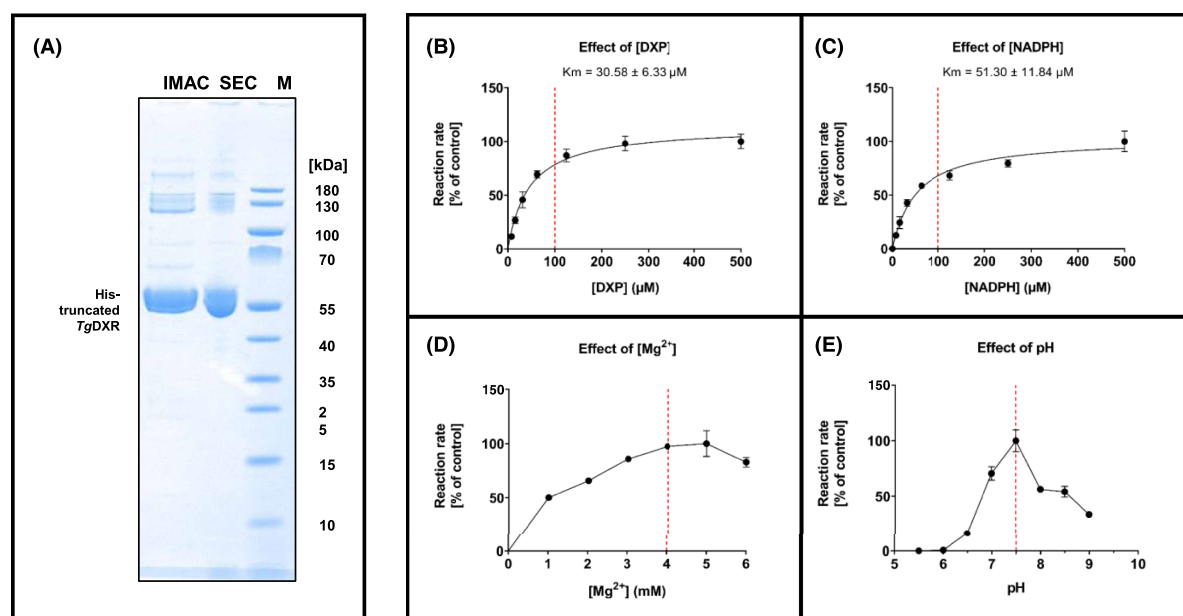

Figure 3. Purification of the His$_{10}$-truncated *Tg*DXR and its optimization and kinetic characterization.
(**A**) SDS–PAGE of samples taken during the purification of truncated His$_{10}$-*Tg*DXR after immobilized metal ion affinity chromatography (IMAC) and size exclusion chromatography (SEC). Marker (M): PageRuler™ Prestained Protein Ladder, Thermo Scientific™, Thermo Fisher Scientific, Waltham, MA, U.S.A., #26616, molecular mass in kDa are indicated. Running Buffer: 20× NuPAGE™ MOPS SDS Running buffer, Thermo Fisher Scientific, Waltham, MA, U.S.A., #NP000102. (**B**) Effects of [DXP] on *Tg*DXR catalyzed reaction. K_m values of DXP and NADPH are shown. (**C**) Effects of [NADPH] on the *Tg*DXR catalyzed reaction. (**D**) Effects of [Mg^{2+}] on the *Tg*DXR catalyzed reaction. (**E**) Effects of pH on the *Tg*DXR catalyzed reaction. See Materials and methods section for the experimental conditions. Optimal and selected concentrations or values are indicated (red line). Data shown are means of four independent experiments, each performed in duplicate ($n = 8$) ± S.D.

The overall structure

The structure of *Tg*DXR was solved and refined to 2.5 Å resolution (data-collection and refinement statistics are summarized in Supplementary Table S2). The asymmetric unit contains one homodimer. The r.m.s. deviation between Cα atom positions within in the two subunits when they are superimposed is 0.3 Å using all 347 Cα atoms. Residues 25–472 could be modelled for both molecules from the electron-density map except the loop ranging from amino acid 182–221 and were therefore not modelled in either of the two subunits. First, we describe the overall structure for monomer A.

*Tg*DXR is composed of three domains: an N-terminal NADPH-binding domain, a connective domain and a C-terminal α-helical domain (Figure 4A). These are arranged in a V shape, where the N-terminal and C-terminal domains form the two arms and the central domain lies at the vertex.

The N-terminal domain (residues 25–171) consists of a Rossmann fold, with a β-sheet containing seven parallel β-strands (β1–β7, including a kink at residue 56 in β2), which is flanked by a total of six α-helices (α1–α6). The N-terminal domain is connected via a long loop (residues 172–227) to the catalytic domain. Of this loop, the largest part is not visible in the electron density and appears to be flexible although NADPH and the inhibitor fosmidomycin are present. The catalytic domain (residues 228–385) includes a four-stranded β-sheet ordered β9–β8–β10–β11, where β10 is positioned antiparallel to the other strands. This sheet adheres to the other two domains by virtue of a layer of helices. β8 extents into a flexible loop consisting of a broken helix α7 which then returns into the four-stranded β-sheet via α helix α8.

The C-terminal domain residues (386–472) feature a four-helix bundle. The dimer interface is created by interactions between the catalytic and connecting regions of each subunit. A twisted eight-stranded β-sheet is formed using the four β-strands of each catalytic domain, with the respective β11 strands positioned antiparallel at its central point (Figure 4B). Further antiparallel interactions between the β12 strands of each subunit are found on the concave surface of this larger sheet; interactions at the C-terminal end of the β12 strand links them to the sheet, thus forming an imperfect ten-stranded β-barrel as the core of the dimer interface.

In the electron density, NADPH could be unambiguously identified and modelled. NADPH is bound to the Rossmann fold by interactions typically observed, while the pyrophosphate moiety interacts with the consensus sequence GGGNGA, establishing further interactions with the co-substrate NADPH which is bound at the identical position as found in other DXR proteins [23,25,41,42]. The binding of the adenine and pentose phosphate moieties of NADPH is identical to that observed in the structure of the *E. coli* DXR, in contrast, the nicotinamide ring of NADPH is ordered in this fosmidomycin complex (Figure 4C).

Fosmidomycin binding site

Within the solvent-shielded cavity that is formed upon closure of the 'lid' residues 281–285 the inhibitor backbone lies parallel to the β-indole of Trp283 at a distance of ~4 Å. The hydroxamic acid moiety of the inhibitor binds to the side-chain of Glu231. The sidechain of Glu231 itself is stabilized and positioned via interaction with Lys299 (Figure 4C). Fosmidomycin further interacts with the sidechains of Asn298 and His280. The sidechain of Glu302 also points towards the fosmidomycin, however the distance is roughly 4 Å indicating a very weak interaction or maybe this interaction is water mediated which cannot be conclusively modelled at this resolution.

SAXS of *Tg*DXR

The *Tg*DXR protein was successfully crystallised and forms a dimeric conformation in solution. However, parts of the protein were not visible in the electron density, likely due to the flexibility, e.g. parts from the N-terminus and more importantly the flexible loop region from the *Tg*DXR protein. These loop regions are special in this *Tg*DXR variant and are not present in homologous structures. We used SAXS to determine the structure of the *Tg*DXR protein in solution. In the SEC-SAXS elution profile (Figure 5A; and Supplementary Figure S2A), *Tg*DXR elutes in one homogenous peak. Evaluation of the data revealed a dimer in solution with the same shape and orientation as determined by X-ray crystallography, with an R_g value of 3.33 nm and a D_{max} value of 10.44 nm (Supplementary Table S3). With the Ensemble Optimisation Method (EOM), we modelled the missing amino acids from the loop region and the N-terminus to each protomer, which completed the structure. The corresponding scattering data with the EOM fit (χ^2: 1.207) is shown in Figure 5B and the most representative EOM model in Figure 5C. The remodelled loops (37 amino acids each), cover the area between both protomers of *Tg*DXR. Its flexibility, evidenced by the absence of electron density in the crystal structure, led us to analyse the loop's position with EOM, resulting in a 62% occupancy in this conformation.
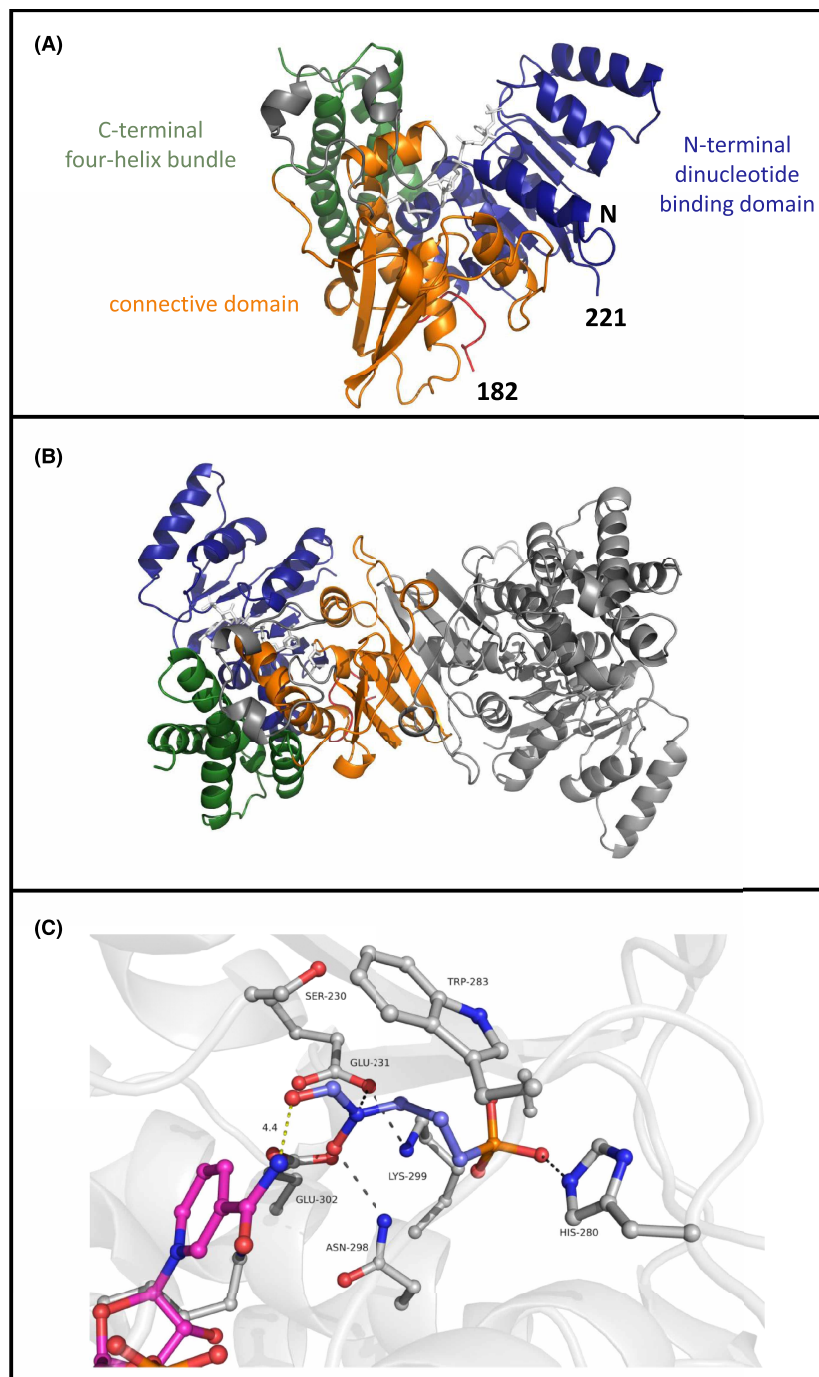
Figure 4. Structure of *Tg*DXR A.

(**A**) Overall structure of *Tg*DXR as observed in the crystal structure. Shown is chain A which is similar to chain B, as calculated by comparing the RMSD of both monomers after superimposing which is 0.3 Å overall. Three different domains are observed and colour coded being the N-terminal nucleotide binding domain (blue) the connective domain (orange) and the C-terminal four helix bundle (green). (**B**) The dimer of *Tg*DXR is highlighted as observed in the asymmetric unit of the crystal. The dimer interface is mediated by the connective domain highlighted in orange in chain A. (**C**) The binding site of fosmidomycin is shown with in ball and stick representation. Fosmidomycin (blue) is bound via interaction with the sidechains of Glu231, His280, and Asn298. All distances are indicated with black line with a maximum distance of 3.6 Å. The distance of fosmidomycin to NADPH (purple) is 4.4 Å, which is too large to allow activity.
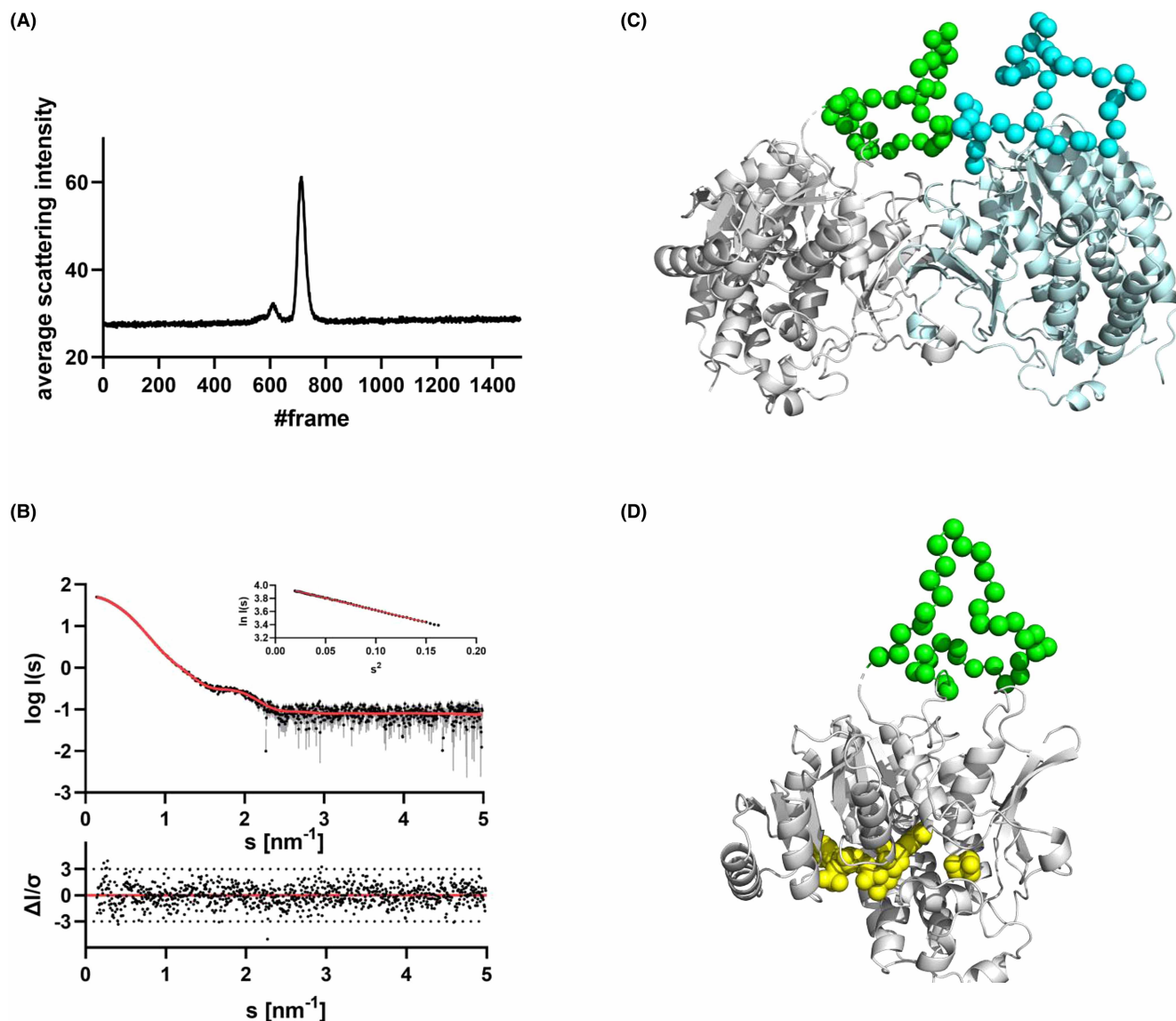
PORTLAND
PRESS

Figure 5. Small-angle X-ray scattering data from *Tg*DXR and the most representative (62%) EOM model.

(**A**) Chromixs SEC SAXS elution profile. Each frame corresponds to 2 s. (**B**) Scattering data of *Tg*DXR. Experimental data are shown in black dots, with grey error bars. The EOM ensemble model fit is shown as red line and below the residual plot of the data is given. The Guinier plot of *Tg*DXR is added in the right corner. (**C**) The rigid body protomers of *Tg*DXR from the crystal are shown in grey and cyan cartoon representation. The determined flexible loop is shown as green and blue spheres. (The other EOM models are part of the Supplementary Information). (**D**) The SAXS completed model of *Tg*DXR is shown as monomer with the flexible loop shown in green spheres. The NADPH and fosmidomycin binding site is highlighted in yellow. It is clear that the flexible loop is remote of the active site and likely serves a more stabilizing role in the dimer of *Tg*DXR.

The loop is located at the back side of the *Tg*DXR protein (Figure 5D) and therefore does not play an immediate role in catalysis.

In vitro biological evaluation
Evaluation of the activity of the *Tg*DXR mutants Glu321Ala, His280Ala and Asn298Ala

To identify the binding site essential for the inhibitory activity of fosmidomycin, we obtained point-mutated *Tg*DXR proteins (section 'Site-directed mutagenesis and expression of *Tg*DXR mutants') and conducted *in vitro Tg*DXR enzyme inhibition assays (section 'Enzymatic assays of *Tg*DXR mutants Glu321Ala, His280Ala

and Asn298Ala'). We compared the reaction rates of *Tg*DXR wild-type with *Tg*DXR mutants Glu231Ala, His280Ala, and Asn298Ala. Unfortunately, the Glu231Ala mutant could not be expressed and therefore the analysis of this mutation was not possible. Both other mutant proteins (His280Ala and Asn298Ala) displayed significantly decreased activities of only 5–6% activity compared with the wild-type DXR protein (Figure 6), indicating that these amino acids are essential for binding of the substrate DXP. This is in line with the DXR protein from *E. coli*, where mutations of the same positions and amino acids also resulted in an almost 19-fold reduction of the activity as observed for the wildtype protein [43]. Due to the low activity, the observed inhibition with fosmidomycin was measured but due to the initial low activity a valid IC_{50} could not be determined for these mutants.

Reverse fosmidomycin thia analogues are potent *Tg*DXR inhibitors

Based on previous studies, demonstrating the effectiveness of reversed hydroxamic acid analogues of fosmidomycin (**1**) as DXR inhibitors, with either a bivalent sulfur or oxygen atom replacing the β-methylene group of the main chain of the linker [34–36], we tested 5 reverse thia (Figure 7, **2–6**) and 4 reverse oxa analogues (Figure 7, **7–10**) for their enzymatic activity against the purified recombinant truncated His_{10}-*Tg*DXR and determined their inhibitory concentrations (IC_{50}) and inhibitory constant (K_i) values.

Interestingly, all the investigated compounds possessed *Tg*DXR inhibitory activity. In particular, the reverse thia isosters revealed a marked increase on the inhibitory activity compared with **1** and the cognate reverse oxa compounds (Figure 8, Table 1 and Supplementary Figure S5). Moreover, the 3,4-difluorophenyl- (**3**) and 3,4-diclorophenyl- (**4**) substituted thia analogues were the most active inhibitors with comparable submicromolar IC_{50} and K_i values (Figure 8, Table 1 and Supplementary Figure S5).

Reverse fosmidomycin analogues inhibit the growth of *T. gondii in vitro*

To determine if reverse thia and reverse oxa analogues of **1** (Figure 7) could inhibit *T. gondii* proliferation *in vitro*, we conducted an evaluation to assess their anti-parasitic activity and their IC_{50} values against the proliferation of *T. gondii* (type II ME49 strain) with an ³[H]-uracil incorporation assay *in vitro*. Interestingly, contrary to **1** that showed no activity accordingly to previous reports [32–37,44]. The *Tg*DXR inhibitors **3**, **4**, **5**, **6**, and **7** demonstrated activity against *T. gondii* growth (Figure 9, Table 2 and Supplementary Figure S6). Moreover, as was first shown in the enzymatic assays, a significant increase in activity for the thia isosters compared with the oxa isoster was observed. Notably, the thia analogue **4** which bears a 3,4-dichlorophenyl moiety in the α-position of the linker demonstrated the most potent inhibitory activity ($IC_{50} = 5.46$ μM) (Figure 9, Table 2 and Supplementary Figure S6).
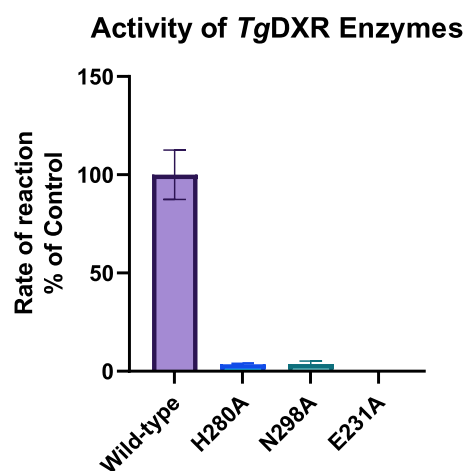

Activity of *Tg*DXR Enzymes

Figure 6. Comparison of the activities of *Tg*DXR wild-type and *Tg*DXR mutants Glu321Ala, His280Ala and Asn298Ala.
Reaction rates of *Tg*DXR **wild-type** (**violet**) and *Tg*DXR mutants **His280Ala** (**H280A, blue**) and **Asn298Ala** (**N298A, green**). **Glu321Ala** (**E321A**) could not be determined. Data shown are from the means of three independent experiments each performed in duplicate ($n = 6$) ± S.D.
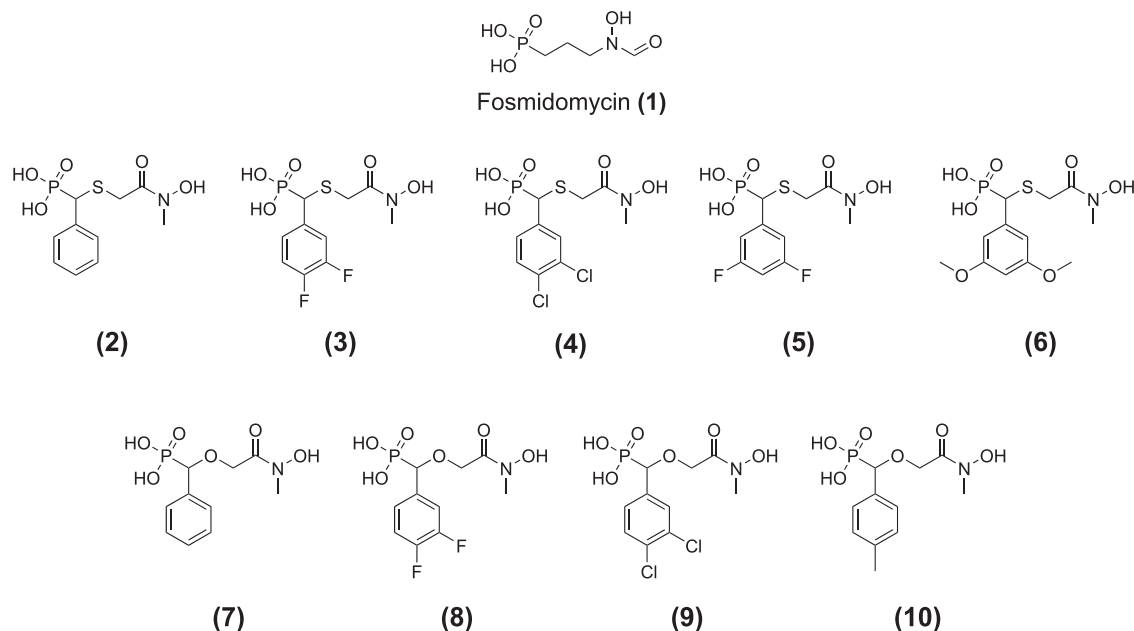
Figure 7. Chemical structures of DXR inhibitors investigated in this study.

Reverse fosmidomycin analogues are not cytotoxic on human host cells

To assess the host cell cytotoxicity of the investigated compounds, MTT assays with Hs27 cells and the *Tg*DXR inhibitors were performed. Similar to **1**, all the reverse thia and oxa analogues did not show any detectable host cytotoxicity at the concentration range of 0.19–200 µM (Figure 9, Table 2 and Supplementary Figure S6). Therefore these *Tg*DXR inhibitors appear to have a good therapeutic index.

Molecular docking of compound 4 into *Tg*DXR

To elucidate a possible binding mode of compound **4** in *Tg*DXR and to predict which enantiomer of **4** could pose the eutomer, the *S*- and *R*-enantiomer of **4** were docked into the X-ray crystal structure of *Tg*DXR from which fosmidomycin was removed. The docking revealed possible binding modes where the *R*-enantiomer of **4** binds outside the fosmidomycin binding pocket whereas the *S*-enantiomer of **4** binds into the binding pocket (Figure 10). In its predicted binding mode, the *S*-enantiomer of **4** binds similarly to fosmidomycin with the phosphonic acid and the hydroxamic acid groups occupying the same positions. The hydroxamic acid group in **4** however is turned compared with fosmidomycin, which might be a result of the change in direction in which this group is attached to the core of **4**. This, however, does not allow for interactions of the carbonyl group with Asn298 of *Tg*DXR in contrast with fosmidomycin. Yet, **4** places the 3,4-dichlorphenyl substituent in a previously unoccupied pocket, which increases the number of hydrophobic interactions to *Tg*DXR, which are important for increasing the affinity with the enzyme.

Discussion

Toxoplasmosis is a widespread disease and current treatment regimens are related to adverse effects and additionally, are not able to eradicate the latent phase of the infection. Thus, the identification of novel drug targets is crucial for the development of novel, potent and safer anti-toxoplasma drugs for improving the health of patients at risk of toxoplasmosis [45]. The MEP pathway has been well established as a promising drug target for novel antimicrobial agents, due to its crucial role on the viability of the microorganism and, additionally, its absence in the human host, that allows the development of selective inhibitors [46].

DXR inhibitors are a class of antimicrobial agents studied intensively in *P. falciparum*, *E. coli* and *M. tuberculosis* [34–36]. From previous SAR studies, it has been shown that the retro-inversion of the hydroxamate moiety of **1** and its N-methylation strongly improve the hydrophobic interaction of Trp212 of *Ec*DXR [47] and that the addition of the α-phenyl substitution of the N-methylated reverse fosmidomycin analogues strongly inhibits the growth of the apicomplexan parasite *P. falciparum* [48,49].
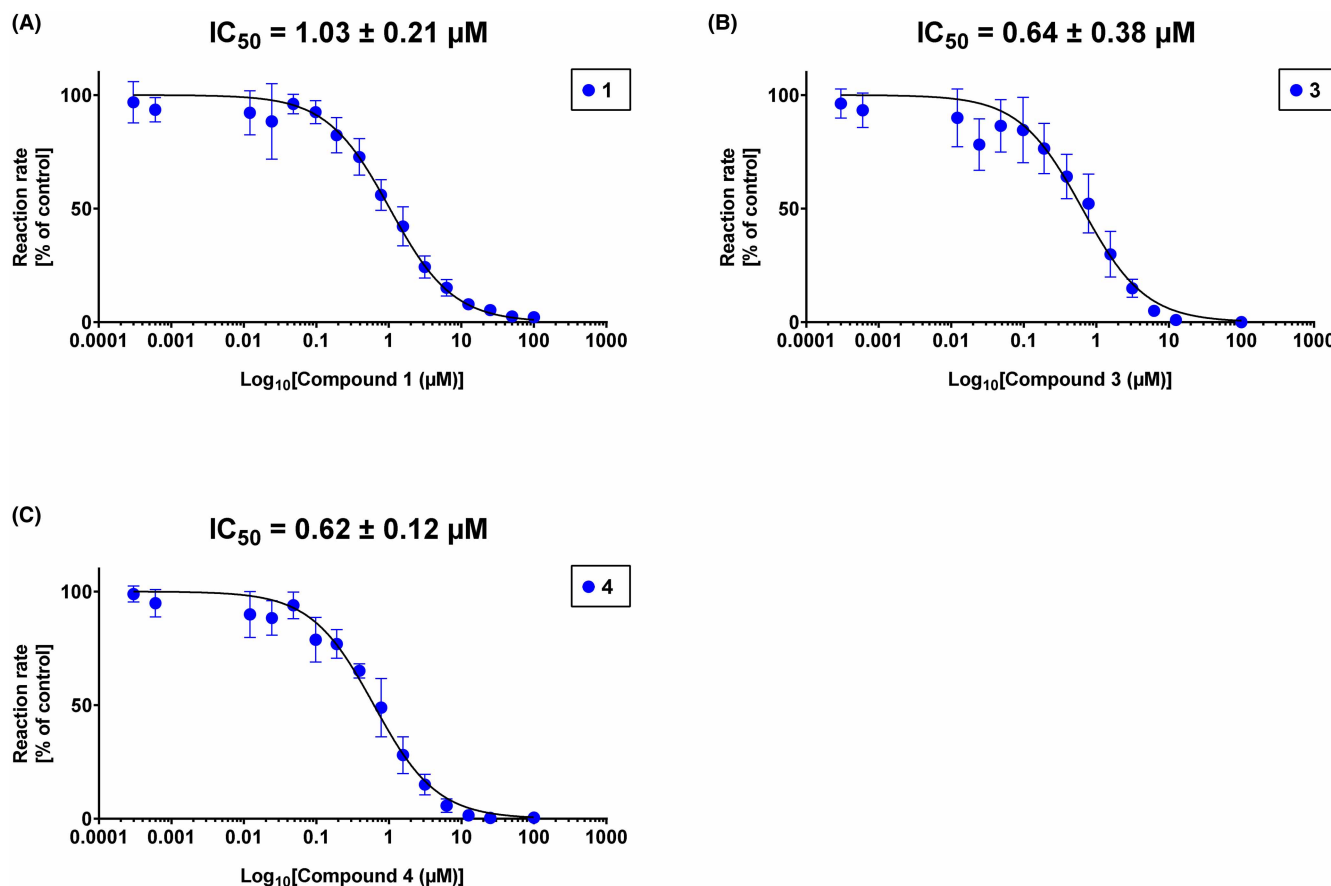
Figure 8. *In vitro* inhibition of *Tg*DXR by most potent DXR inhibitors.

The enzymatic inhibitory activity of 1 (**A**), 3 (**B**) and 4 (**C**) were determined by enzymatic assays *in vitro*. Assays were performed in 96 well plates at 30°C, containing 100 nM of purified *Tg*DXR protein in dimeric state, 100 μM of NADPH and 4 mM of MgCl$_2$ as cofactors, 100 μM of DXP as substrate in 50 mM HEPES buffer (pH 7.5) containing 50 μg/ml of bovine serum albumin (BSA). The investigated compounds were tested in a concentration range of 3.05 nM to 100 μM. Data shown are from the means of three independent experiments each performed in duplicate ($n = 6$) $\pm$ S.D. IC$_{50}$ values of each compound are shown.

DXR inhibitors against *T. gondii* have been already investigated by Cai et al. [37], precisely α-phenyl and α-pyridine substituted fosmidomycin analogues, pyridine containing phosphonate compounds, non-hydroxamate phosphonate inhibitors containing a pyridine and 1-hydroxy-5-phenylpyridin-2-one moiety without a phosphonate group. All the compounds were active against *Tg*DXR, but none of them inhibited the parasite growth, probably due to the permeability barrier posed by parasite plasma membrane(s) of *T. gondii* that is lacking the fosmidomycin transporter GlpT [33].

In this study, we present the first crystal structure of *Tg*DXR in the tertiary complex with NADPH and fosmidomycin. No magnesium ion was observed in this structure despite the fact that it is essential for activity and was included in the crystallization experiments, which also was the case for the *E. coli* DXR protein [23]. The overall structure of *Tg*DXR resembles its counterparts in various species [23,25,40,41]. A search for homologous structures revealed that overall the DXR protein are very similar, with an r.m.s.d. of 1.2–1.8 Å for the overall structure (calculated using the EBI fold server). This shows that the overall fold is conserved. Furthermore, also the amino acids involved in DXP substrate binding and conversion are conserved among the different enzymes. Not surprisingly, also the binding site for fosmidomycin at *Tg*DXR consists of the same amino acids as seen in the structure of the *Ec*DXR, indicating that the domain of *Tg*DXR is similar to the *Ec*DXR domain (Figure 4C). The distance of the hydroxymate region of fosmidomycin to NADPH is 4.4 Å, which is too large for conversion (indicated by the yellow line in Figure 4C). With the substrate DXP, the distance to NADPH is reduced, as an additional bond length is strategically positioned to facilitate the occurrence

Table 1. *In vitro* activity (IC$_{50}$ and K_i values) of DXR inhibitors against *Tg*DXR enzyme.

Compound	IC$_{50}$ ± S.D. (μM)	K_i (μM)
1	1.03 ± 0.21	0.31[a]
2	1.23 ± 0.12	0.37
3	0.64 ± 0.38	0.19
4	0.62 ± 0.12	0.19
5	2.45 ± 0.54	0.74
6	3.90 ± 1.06	1.18
7	5.82 ± 1.52	2.69
8	52.14 ± 0.34	11.00
9	2.44 ± 0.43	0.74
10	7.68 ± 0.87	2.51

[a]The K_i value reported in previous studies is 0.09 μM [37]. Values shown in the table represent the means of three independent experiments each done in duplicate ($n = 6$) ± S.D.

of the reaction. Since the structure is of medium resolution, we could not identify water molecules with certainty, likely however they play a role in catalysis as shown before [23]. Moreover, the parts of the protein that were not visible in the electron density were determined through SAXS, unveiling their peculiarity. With SAXS however only the position of the C-α atoms can be determined, and atomic detail of the side chains is still lacking which would allow a more detailed description.

In addition, we performed a biological investigation on *Tg*DXR, repurposing already investigated reverse α-phenyl-β-oxa and β-thia-substituted analogues of (**1**) which were previously described as potent inhibitors of *P. falciparum*, *E. coli* and *M. tuberculosis* DXR enzymes [34–36]. We show that all the investigated compounds possess *Tg*DXR inhibitor activity, with the reverse thia analogues presenting a more pronounced activity than the reverse oxa analogues. Moreover, we noticed that inhibitors with a the 3,4-halogen substitution of the phenyl moiety of the reverse thia analogues confers the highest potency against the enzymatic activity of *Tg*DXR (Figure 8, Table 1 and Supplementary Figure S5). In the cell-based assays, we demonstrated that the *Tg*DXR inhibitors **3**–**7** inhibit *T. gondii* proliferation in contrast with **1** (Figure 9, Table 2 and Supplementary Figure S6). As shown in previous studies, *T. gondii* is unaffected by the activity of compound (**1**) probably due to its lack of the GlpT transporter, the glycerol-3-phosphate (G3P) transporter responsible for the drug uptake of (**1**) in *E. coli* [31,33]. *T. gondii* does not possess a protein with significant sequence similarity to *E. coli* GlpT. This suggests that the activity of the derivatives of (**1**) on *T. gondii* may be due to the use of a different transporter protein or their increased lipophilicity, as indicated by their higher ClogP values compared with (**1**) in Figure 11, that could facilitate passive transport through the membranes [50].

*Tg*PiT and *Tg*PT2 are plasma membrane transporters found in *T. gondii*. Notably, *Tg*PT2, which is only present in coccidian parasites, is essential for parasite growth. These proteins, possessing phosphate transport activities [51], could be potential candidates for transporting reverse fosmidomycin derivatives.

Additionally, we observed once again a trend within the thia analogues, showing higher potency compared with the cognate oxa analogues. Previous studies showed that the increased activity of the α-phenyl-β-thia-substituted analogues against *Ec*DXR and *Mt*DXR enzymes is attributed to the interaction of the sulfur atom with the conserved Met298 within the flexible loop of the enzymes [34,48,50]. Furthermore, in this context, the 3,4-dichlorophenyl substituted compound **4** emerged as the most potent one in inhibiting *T. gondii* proliferation, with an IC$_{50}$ of 5.46 μM, presumably due the improved lipophilicity provided by the 3,4-dichlorophenyl substitution (Figure 11) that enhances cellular uptake [52].

Conclusions

In summary, in the present study we report the first X-ray structure of *Tg*DXR co-crystallized with fosmidomycin and the cofactor NADPH and its biochemical characterization, as well as the identification of reverse
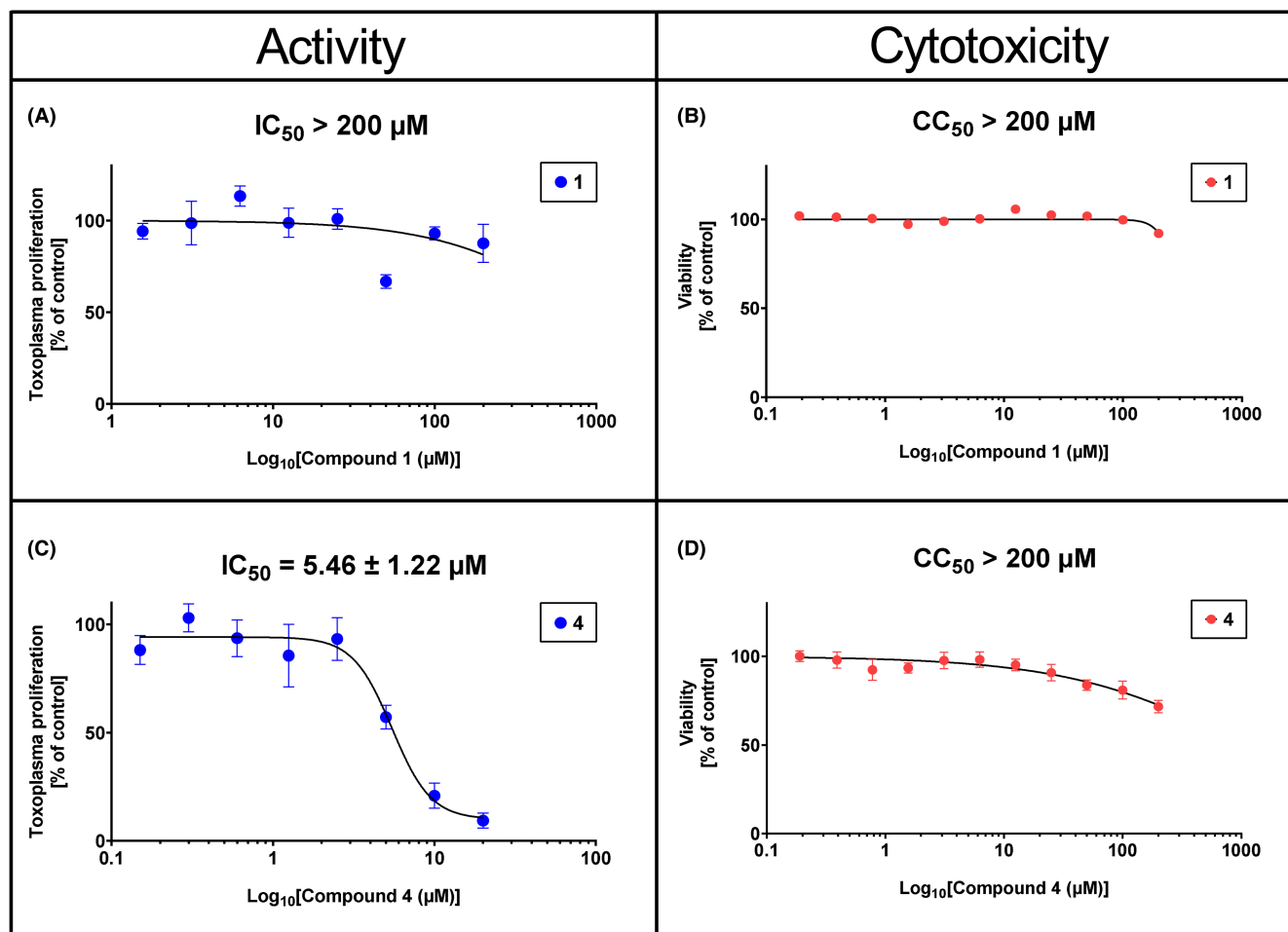
Figure 9. Anti-toxoplasma activity and cytotoxicity on human fibroblasts Hs27 of fosmidomycin and the 3,4-dichlorophenyl-thia analogue.
The antiprotozoal activity of 4 (**A**) was determined by the *T. gondii* inhibition assay via the amount of [^{3}H]-uracil incorporation into the RNA of the parasite *in vitro*. Cytotoxicity of 4 (**B**) was measured by MTT assays on human fibroblasts Hs27. Data shown are the means of three independent experiments each performed in duplicate ($n = 6$) ± SEM. IC$_{50}$ ± S.D. and CC$_{50}$ values of compound **4** are shown.

α-phenyl-β-thia- and β-oxa-isosters of fosmidomycin as novel anti-*T. gondii* agents with in part potent *Tg*DXR inhibitory activity. The ternary co-crystal structure of *Tg*DXR and **1** will serve as starting points for the design and development of improved *Tg*DXR inhibitors. Further efforts are needed for the development of enhanced derivatives and to explore the efficacy *in vivo*.

Material and methods
Biochemical characterization
Sequence alignment
The amino acid sequence of the investigated protein *Tg*DXR (NCBI Reference Sequence: XP_018635719.1) was compared with a multiple sequence alignment using Clustal Omega sequence analysis tool (https://www.ebi.ac.uk/Tools/msa/clustalo/) [53] with its default settings with DXR enzymes from other species that have been extensively studied: *P. falciparum* DXR (*Pf*DXR, NCBI Reference Sequence: AAD03739.1), *M. tuberculosis* DXR (*Mt*DXR, NCBI Reference Sequence: OHO19719.1) and *E. coli* DXR (*Ec*DXR, NCBI Reference Sequence: WP_302347400.1) and visualized and the percentage of identity analysed with Jalview software version 2.11.2.7 [54] (Supplementary Figure S1).

PORTLAND PRESS

Table 2. *In vitro* activity of *Tg*DXR inhibitors and pyrimethamine against *T. gondii* ME49 tachyzoites and their cytotoxicity on human fibroblasts Hs27.

Compound	IC$_{50}$ ± S.D. (µM)	CC$_{50}$ (µM)
1	>200	>200
2	>100	>200
3	14.39 ± 1.94	>200
4	5.46 ± 1.22	>200
5	55.99 ± 6.11	>200
6	12.51 ± 5.56	>200
7	48.20 ± 8.56	>200
8	>100	>200
9	>100	>200
10	>100	>200
Pyrimethamine	0.22 ± 0.05	>100

Values shown in the table represent the means of three independent experiments each done in duplicate (*n* = 6) ± S.D. Pyrimethamine was used as anti-toxoplasma reference compound.

*Tg*DXR

The gene of 1-Deoxy-D-xylulose 5-phosphate reductoisomerase of *T. gondii* (*Tg*DXR) ME49 strain was identified using *ToxoDB database* (http://ToxoDB.org). The gene of *Tg*DXR (NCBI: NC_031478.1), optimized for expression in *E. coli*, was obtained from GenScript (Piscataway, Township, NJ, U.S.A.) as a synthetic gene subcloned into the pET-16b plasmid, using NdeI/BamHI restriction sites. The resulting expressed protein carries
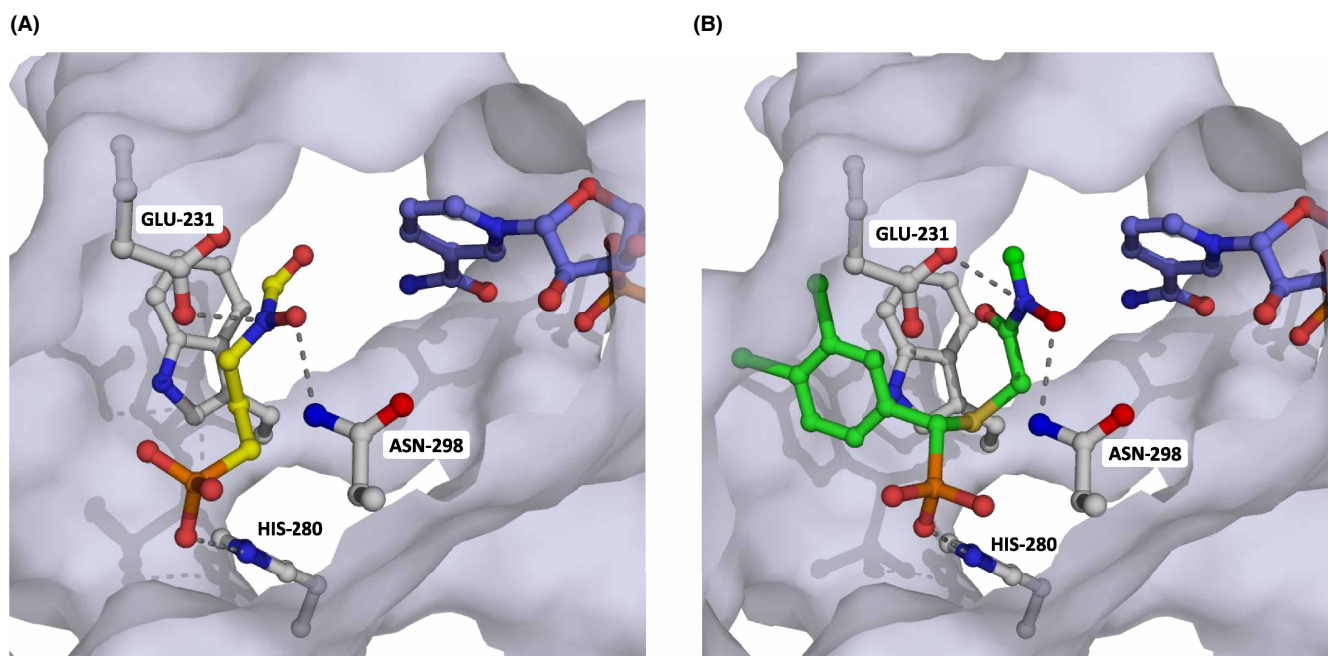
(A)

(B)

Figure 10. Predicted binding modes of compound 4 in the X-ray crystal structure of *Tg*DXR.
(**A**) The fosmidomycin binding site is illustrated, with fosmidomycin represented as yellow sticks, interacting with Glu231, Asn298, and His280.
(**B**) Docking results for compound **4** reveal that the 3,4-dichlorophenyl substituent binds in a previously unoccupied pocket.
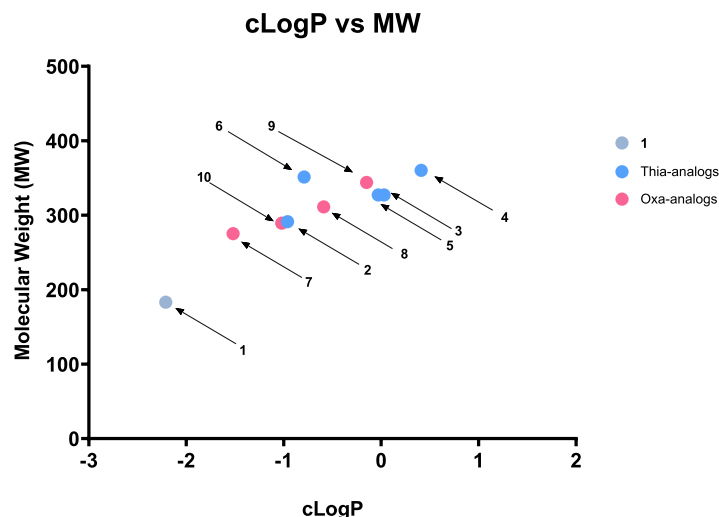
Figure 11. Plot of ClogP vs. MW for fosmidomycin and its thia- and oxa-analogs.
Fosmidomycin (**1**) is shown in grey, the thia-analogs in blue, and the oxa-analogs in pink. The investigated fosmidomycin derivatives exhibit increased lipophilicity compared with **1**, with compounds **3** and **4**, the most active compounds, being the most lipophilic. Clog*P* values have been predicted using the Marvin JS calculator.

an N-terminal decahistidine tag (His$_{10}$). However, the purification of the recombinant His$_{10}$-tagged *Tg*DXR proved to be challenging. To overcome these issues and to generate a soluble recombinant protein, another expression plasmid was designed. We deleted 181 amino acids (2–182) of the *Tg*DXR sequence representing the bipartite apicoplast targeting peptide [37] in order to generate a soluble truncated His$_{10}$-tagged *Tg*DXR containing the sequence of the catalytic domain (Supplementary Figure S1).

Cloning of truncated His$_{10}$-*Tg*DXR and construction of the expression plasmid

The generation of the truncated His$_{10}$-*Tg*DXR commenced with the deletion of 181 amino acids via Site-Directed-Mutagenesis method [55]. For this purpose, the coding sequence of the truncated *Tg*DXR was amplified from the pET-16b plasmid construct with a polymerase chain reaction (PCR) (Phusion® High-Fidelity PCR Kit, New England BioLabs, Frankfurt am Main, Germany, #E0553S) using the primers *Tg*DXR-del181AA_For and *Tg*DXR-del181AA_REV (Supplementary Table S1). Then, the coding sequence was purified through an 1% agarose gel purification [56] and ligated with a KLD- Enzyme Mix (KLD Enzyme Mix, New England BioLabs, Frankfurt am Main, Germany, #M0554S). Subsequently the plasmids were transformed into an *E. coli* DH5α (DH5α Competent Cells, Thermo Fisher Scientific, Waltham, MA, U.S.A., #EC0112), which then were streaked onto Luria-Bertani (LB) agar-plates containing ampicillin (100 µg/ml) (Ampicillin, Thermo Fisher Chemicals, Thermo Fisher Scientific, Waltham, MA, U.S.A., #J60977.14). To confirm the successful cloning, positive clones were identified through PCR. Additionally, DNA sequencing was performed using T7 forward and reverse primers for further verifications. The *Tg*DXR expression plasmid was extracted with a plasmid miniprep kit (Monarch® Plasmid Miniprep Kit, New England BioLabs, Frankfurt am Main, Germany, #T1010L).

Expression of truncated His$_{10}$-*Tg*DXR

The expression plasmid *Tg*DXR was transformed into the chemically competent *E. coli* BL21 (DE3) cells (BL21 (DE3) Singles™ Competent Cells — Novagen, Merck KGaA, Darmstadt, Germany, #70235). Then *E. coli* transformants were streaked onto LB agar-plates containing ampicillin (100 µg/ml) (Ampicillin, Thermo Fisher Chemicals, Thermo Fisher Scientific, Waltham, MA, U.S.A., #J60977.14) and incubated overnight at 37°C.

To express the His-tagged protein, 100 ml overnight pre-cultures were prepared using fresh colonies from LB agar plates or 50% glycerol cryo stock stored at −80°C. The day after, 1 l of freshly prepared and autoclaved LB media (10 g Triptone, 5 g yeast extract and 5 NaCl) was supplemented with 100 µg/ml of ampicillin and inoculated with the pre-cultures to an optical density at 600 nm (OD$_{600}$) of 0.1. The main culture was then incubated with shaking at 37°C and 180 rpm. At an OD$_{600}$ of 0.6, protein expression was induced with the supplementation in the culture of isopropyl-β-D-thiogalactopyranosid (IPTG, Merck KGaA, Darmstadt, Germany, #I6758)

to a final concentration of 1 mM. The main culture was further incubated for additional 2 h with shaking at 37°C and 180 rpm. Afterwards, cells were harvested via centrifugation at 5000g, for 15 min at 4°C (rotor SLC-6000, Sorvall, Thermo Fischer, Waltham, MA, U.S.A.), the supernatant discarded. The cell pellet was used subsequently or snap frozen in liquid nitrogen and short-term stored at −20°C.

Purification of truncated His$_{10}$-*Tg*DXR

Truncated His$_{10}$-*Tg*DXR purification involved two main steps: immobilized metal ion affinity chromatography (IMAC) and SEC.

Cells were thawed at 4°C and suspended with ice-cold lysis buffer A (50 mM NaH$_2$PO$_4$, 300 mM NaCl, 20 mM imidazole, pH 8) supplemented with protease inhibitor cocktail (cOmplete Protease Inhibitor Cocktail, Roche, Basel, Switzerland). Subsequently, cell lysis was performed through the application of shear force using a cell disruptor/homogenizer (M-110P Microfluidizer, Microfluidics Inc., Westwood, MA, U.S.A.). This method was employed to effectively break down the cells and release their content. To eliminate cell membranes and other insoluble detritus, ultracentrifugation of the lysate was performed at 100,000g, for 45 min at 4°C (Beckman Optima XE, Beckman Coulter Inc., Brea, CA, U.S.A.). Then, the collected supernatant was purified via Ni-IMAC at 4°C on a Ni^{2+} pre-treated HiTrap IMAC FF 5 ml column (Cytiva Life Science, Marlborough, MA, U.S.A., #17092104) using a protein purification system (Äkta Purifier 10, GE Healthcare, Chicago, IL, U.S.A.). The protein was loaded on the column with a flow rate of 1 ml/min. After binding, the resin was washed with buffer B (50 mM NaH$_2$PO$_4$, 150 mM NaCl, 20 mM imidazole, pH 8) to remove the non-specifically bound proteins. Afterwards, the protein was eluted with a gradually increasing concentration of imidazole with buffer C (50 mM NaH$_2$PO$_4$, 150 mM NaCl, 300 mM imidazole, pH 8). As determined by absorption at λ 280 nm, the fractions containing proteins were then pooled, concentrated, and subjected to a SEC to further improve its purity. SEC was performed on an Äkta Purifier 10 equipped with a pre-equilibrated Superdex 200 Increase 10/300 GL column (Cytiva Life Science, Marlborough, MA, U.S.A., #28990944) at a flow rate of 0.5 ml/min with buffer D (20 mM Tris–HCl, 150 mM NaCl, 2% Glycerol, pH 7.5). Dimeric protein was collected, concentrated, aliquoted, and snap-frozen for storage at −80°C.

Determination of protein concentration

The concentration of the protein was assessed by measuring its absorbance with a microvolume UV-Vis spectrophotometer (NanoDrop™ One, Thermo Fisher Scientific, Waltham, MA, U.S.A.) using protein-specific parameters, including the molecular mass (51,808 Da) and the extinction coefficient of the protein (34,420 M^{-1} cm^{-1}) obtained with the web-software tool Expasy ProtParam [57].

T. gondii DXR enzyme kinetic characterization and optimization

To biochemically characterize the catalytic ability of the truncated *Tg*DXR for the conversion of DXP into MEP in the presence of the cofactors Mg^{2+} and NADPH, and to determine the optimum conditions for maximum enzyme activity, the enzymatic assays were monitored at 340 nm (maximal absorbance of NADPH) in different conditions.

The enzymatic activity was evaluated in fixed conditions, using 50 mM HEPES buffer containing 50 μg/ml of bovine serum albumin (BSA) containing 100 nM of purified *Tg*DXR protein in dimeric state. In each experimental evaluation, only one parameter was varied: either the substrate (DXP) concentration (ranging from 7.8 to 500 μM), or the cofactor NADPH (ranging from 7.8 to 500 μM), or Mg^{2+} concentration (ranging from 1 to 6 mM) or the pH (ranging from 5.5 to 9) (Figure 3).

For the determination of the kinetic parameters, various concentration of the substrate DXP or NADPH were employed for the determination of the apparent K_m (substrate concentration that yield a half-maximal velocity) and V_{max} (maximum velocity) for the enzyme. These parameters were calculated by a non-linear regression with the software GraphPad PRISM™ (Version 9.5.1; San Diego, CA, U.S.A.) plotting the initial velocity of the reactions and using the Michaelis–Menten model (Figure 3).

Site-directed mutagenesis and expression of *Tg*DXR mutants

Site-directed mutagenesis of the truncated His$_{10}$-*Tg*DXR was performed on the pET16-b plasmid (see above) using the Site-Directed-Mutagenesis method in order to generate Glu231Ala, His280Ala, and Asn298Ala mutants. Briefly, the coding sequence of truncated *Tg*DXR was amplified from the pET-16b plasmid using PCR with primers reported in Supplementary Table S2. The amplified sequence was purified via 1% agarose gel and

ligated using KLD Enzyme Mix. The plasmids were then transformed into *E. coli* DH5α cells and streaked onto LB agar plates with ampicillin (100 μg/ml). Positive clones were confirmed by PCR and further verified by DNA sequencing using T7 primers. Finally, the *Tg*DXR expression plasmid was extracted using the Monarch® Plasmid Miniprep Kit. The mutant *Tg*DXR plasmids were used to transform *E. coli* BL21 (DE3) competent cells for expression under conditions identical to those used for wild-type expression. Cells were cultured at 37°C in LB medium with shaking until reaching an optical density at 600 nm of 0.6. Protein expression was induced with 1 mM IPTG, followed by an additional 3-h incubation at 37°C. Cells were harvested by centrifugation (5000g for 15 min at 4°C) and stored at −80°C until needed. The histidine-tagged proteins were subsequently purified as described for the wild-type protein (see section 'Purification of truncated His$_{10}$-*Tg*DXR'). Structural characterization of the *Tg*DXR catalytic domain.

Crystallization and structure determination of *Tg*DXR

*Tg*DXR was crystallized by sitting-drop vapor-diffusion at 12°C at a concentration of 7–10 mg/ml with 20 mM TRIS pH 7.5, 150 mM NaCl, 2% glycerol containing 1 mM fosmidomycin, 4 mM MgCl$_2$ and 4 mM NADPH. Crystals formed after a couple of days, were cryo-protected with 20% ethylene glycol, washed in mineral oil and flash frozen in liquid nitrogen. Diffraction data were collected at 100 K at beamline ID30-B (ESRF, Grenoble, France) using a 0.9793 Å wavelength. Data reduction was performed using XDS [58] and aimless [59] from the CCP4 suite [60]. The structure was solved via molecular replacement with Phaser [61]. The initial model was refined alternating cycles of manual model building in COOT [62,63] and automatic refinement using Phenix [64] version 1.19.2_4158. Data collection and refinement statistics are reported in Supplementary Table S2.

SAXS from *Tg*DXR

We collected the SEC-SAXS data on beamline BM29 at the ESRF Grenoble [65,66]. The BM29 beamline was equipped with a PILATUS 2M detector (Dectris) at a fixed distance of 2.827 m.

The SEC-SAXS measurement was performed at 10°C with a *Tg*DXR protein concentration of 8.00 mg/ml. The SEC-SAXS run was performed on a Superdex 200 increase 10/300 column (300 μl inject, buffer: 20 mM Tris–HCl, 150 mM NaCl, 40 mM MgCl$_2$, 2% glycerol, pH 7.5) with a flowrate of 0.5 ml/min. We collected 1500 frames with an exposer time of 2 s/frame and scaled the data to absolute intensity against water.

All used programs for data processing were part of the ATSAS Software package (Version 3.0.5) [67]. Primary data reduction was performed with the programs CHROMIXS [68] and PRIMUS [69]. With the Guinier approximation [70], we determined the forward scattering $I(0)$ and the radius of gyration (R_g). The program GNOM [71] was used to estimate the maximum particle dimension (D_{max}) with the pair-distribution function $p(r)$. We used the partially solved crystal structure as template in an EOM [72,73] and added the missing amino acids from the loop region and the N-terminus to each protomer.

Molecular docking of compound 4 into *Tg*DXR

For the molecular docking the two enantiomers of compound **4** were drawn and converted into 3D using the ChemDraw19 suite. The enantiomers of **4** were subsequently docked into the X-ray crystal structure of DXR from which **1** was removed utilizing a combination of AutoDock as a docking engine and the DrugScore2018 distance-dependent pair-potentials as an objective scoring function [74,75]. During docking, default parameters were used, except for the clustering RMSD cut-off, which was set to 2.0 Å [74–76]. The docking grids were centred on the **1** binding site. Binding modes were considered valid if they were contained in the largest cluster with the most favourable docking energies, which comprised at least 20% of all docking poses.

Visualization and analysis of molecular structures

For figure preparation of the crystal structures of *Tg*DXR enzyme we utilized PyMOL software suite (www.pymol.org) [77].

In vitro biological evaluation

Compounds

Fosmidomycin (**1**) (Fosmidomycin sodium salt, Invitrogen, Thermos Fisher Scientific, Waltham, MA, U.S.A., #FR-31564) was dissolved in Dulbeccós Phosphate Buffered Saline ((1x), Gibco-Thermo Fisher Scientific, Waltham, MA, U.S.A., #14190144). DXR inhibitors (((2-(hydroxy(methyl)amino)-2-oxoethyl)thio)(phenyl)

methyl)phosphonic acid (**2**); ((3,4-difluorophenyl)((2-(hydroxy(methyl)amino)-2-oxoethyl)thio)methyl)phosphonic acid (**3**), ((3,4-dichlorophenyl)((2-(hydroxy(methyl)amino)-2-oxoethyl)thio)methyl)phosphonic acid (**4**), ((3,5-difluorophenyl)((2-(hydroxy(methyl)amino)-2-oxoethyl)thio)methyl)phosphonic acid (**5**), ((3,5-dimethoxyphenyl)((2-(hydroxy(methyl)amino)-2-oxoethyl)thio)methyl)phosphonic acid (**6**), ((2-(hydroxy(methyl)amino)-2-oxoethoxy)(phenyl)methyl)phosphonic acid (**7**), ((3,4-difluorophenyl)(2-(hydroxy(methyl)amino)-2-oxoethoxy)methyl)phosphonic acid (**8**), ((3,4-dichlorophenyl)(2-(hydroxy(methyl)amino)-2-oxoethoxy)methyl)phosphonic acid (**9**), ((2-(hydroxy(methyl)amino)-2-oxoethoxy)(p-tolyl)methyl)phosphonic acid (**10**) employed in this study (Figure 7) were prepared using procedures from previously published methods [34–36] and dissolved in DMSO (dimethyl sulfoxide, ≥99%, Thermo Scientific Chemicals, Waltham, MA, U.S.A., #A12380.36). Staurosporine (Merck, Darmstadt, Germany, #S4400) and pyrimethamine (Merck, Darmstadt, Germany, #219864) were dissolved in DMSO. All the compounds were prepared as 10 mM stock solutions and stored at −20°C. Before use, these solutions were thawed and diluted in culture medium to produce the appropriate concentrations (ranging from 0.0003 to 200 μM).

T. gondii DXR enzyme inhibition assays

The enzymatic assays were conducted at 30°C in 96 well plates using a total reaction volume of 150 μl containing 100 nM of purified TgDXR protein in dimeric state, 100 μM of NADPH and 4 mM of $MgCl_2$ as cofactors, 100 μM of DXP as substrate in 50 mM HEPES buffer (pH 7.5) containing 50 μg/ml of BSA. For the screening, DXR inhibitors were tested for their inhibitory activity and their IC_{50} measurements at concentrations ranging from 100 μM to 3.05 nM, in dilution steps 1:2.

To optimize and to ensure the interaction of NADPH and its enzyme binding pocket, the assay solution was incubated for 10 min at 37°C. Then, the reaction was commenced with the addition of 100 μM of DXP to the complete assay mixture. The reaction was monitored by measuring the absorption at 340 nm every minute for 1 h using a microplate reader (Tecan® 200 Pro, Tecan Group, Männedorf, Switzerland). The initial velocity of the reactions were calculated, the values were then used in the software GraphPad PRISM™ (Version 9.5.1; San Diego, CA, U.S.A.) for determinations of the IC_{50} values. The inhibitor constant values (K_i) of all inhibitors were determined using the Michaelis–Menten formula $K_i = IC_{50}/(1 + [S]/K_m)$, [S] is the concentration of DXP (100 μM) and K_m was calculated as 30.58 μM.

Enzymatic assays of TgDXR mutants Glu321Ala, His280Ala and Asn298Ala

After purifying the TgDXR mutants Glu321Ala, His280Ala and Asn298Ala, their activities were tested in comparison with the TgDXR wildtype. Enzymatic assays were conducted under the same conditions described in section 'T. gondii DXR enzyme inhibition assays'.

T. gondii and host cells in vitro culture

T. gondii tachyzoites of the ME49 strain (ATCC/LGC Standards GmbH, Wesel, Germany, #50611), were cultured and maintained by repeat passage in monolayers of human foreskin fibroblasts Hs27 (ATCC/LGC Standards GmbH, Wesel, Germany, #CRL-1634) as host cells. Cultures were grown in Iscove's modified Dulbecco's medium (IMDM; Gibco-Thermo Fisher Scientific, Waltham, MA, U.S.A., #12440053) supplemented with 10% heat-inactivated fetal bovine serum (FBS Standard; South America origin, FBS, 2 μm sterile filtered, PAN-Biotech, Aidenbach, Germany, #P30-3306) and 50 mM 2-mercaptoethanol (Gibco-Thermo Fisher Scientific, Waltham, MA, U.S.A., #21985023) at 37°C and 5% CO_2 as previously described [78–80].

T. gondii in vitro growth assay

With the aim to assess the inhibitory in vitro effect on parasite growth, T. gondii growth assays were performed as described previously [78–80]. Compounds, previously diluted in culture media in appropriate stock solutions, were added to confluent monolayers of Hs27 cells in 96-flat well plates at various concentrations. Then, freshly harvested tachyzoites were added to the cultures at a multiplicity of infection of 1:1 (parasite/host cell ratio). As controls, untreated and uninfected Hs27 cells, 24 h pre-stimulated and T. gondii infected cells with human interferon γ (IFN γ) (300 U/ml) (Merck, Darmstadt, Germany, #I17001) and T. gondii infected cells only were employed. After 48 h incubation, proliferating toxoplasmas were labelled with 0.3 μCi/well of tritiated uracil (^{3}H-U; 5 mCi, Hartmann Analytic, Braunschweig, Germany, #ART1782) [81]. After 28–30 h of incubation, plates were frozen at −20°C overnight. Cells were then thawed and harvested (Basic96 Harvester; Zinsser Analytic, Skatron Instruments, Northridge, CA, U.S.A.), purified with glass fibre filters (Printed Filtermat A 102 mm ×

258 mm; PerkinElmer, Waltham, MA, U.S.A.) and dried at 130°C for 15–20 min. Dried filters were then wrapped into transparent plastic covers, dunked with 10 ml scintillation cocktail (Betaplate Scint; PerkinElmer, Waltham, MA, U.S.A., #1205-440), sealed and then loaded into metal cassettes and the incorporation of ^{3}H-uracil into the RNA of proliferating toxoplasmas was measured using a β-counter, a liquid scintillation counter that measure the Cherenkov radiation (Betaplate Liquid Scintillation Counter 1205; LKB-WALLAK, Melbourne, Australia). All data sets were normalized to 100% of the positive control. The dose-response curves of the compounds were fitted by means of the statistics software GraphPad PRISM™ (Version 9.5.1; San Diego, CA, U.S.A.). The minimal concentrations of compounds required for 50% inhibition of the parasite (IC_{50} values) were determined by non-linear regression analysis. Pyrimethamine [13,82] was used as reference anti-toxoplasma compound.

Cytotoxicity assays

The method based on the reduction of the tetrazolium dye MTT [3-(4,5-dimethylthiazole-2-yl)-2,5-diphenyltetrazolium bromide] to its purple insoluble formazan by mitochondrial NAD(P)H-dependent cellular oxidoreductase enzymes in living cells, previously described by Mosmann [83] was employed to assess the cytotoxic effects of the examined DXR inhibitors on the host cells, as previously described [78–80]. Briefly, Hs27 cells were cultured in 96-well plates at a concentration of 5×10^4/well in (IMDM, Gibco–Thermo Fisher Scientific, Waltham, MA, U.S.A., #12440053) with a volume of 100 μl per well and incubated at 37°C overnight. Then, eleven two-fold serially diluted concentrations of the investigated compounds ranging from 200 to 0.09 μM were prepared and added to each well. Hs27 cells were then incubated for 24 h in humidified atmosphere of 5% CO_2 in air. Controls included wells containing medium alone without cells (blank), untreated Hs27 cells, DMSO (negative control) and staurosporine (0.031, 0.062, 0.125, 0.25, 0.5, 1 μM) (Merck, Darmstadt, Germany, #S4400) as apoptosis inducer [84]. After incubation, the culture media was replaced with 100 μl of DMEM medium without phenol (Gibco-Thermo Fisher Scientific, Waltham, MA, U.S.A., #21041025) plus 10% heat-inactivated (FBS Standard, South America origin, FBS, 2 μm sterile filtered, PAN-Biotech, Aidenbach, Germany, #P30-3306), and 50 mM 2-mercaptoethanol (Gibco-Thermo Fisher Scientific, Waltham, MA, U.S.A., #21985023). Thereafter, the MTT reagent was added to each well and analysis conducted following the manufacture instructions (CyQuant MTT Cell Viability Assay Kit, Thermo Fisher Scientific, Waltham, MA, U.S.A., #V-13154). The absorbance was measured at 570 nm on an ELISA microplate reer (TECAN Sunrise, Männedorf, Switzerland) and the percentage of viability was calculated when compared with the untreated control. The data set was subsequently adjusted by applying blank correction. Cell viability values expressed as percentage of the negative control value were calculated as follows:

$$\% \text{ Cell viability} = \frac{\text{mean absorbance of treated wells} - \text{blank}}{\text{mean absorbance of negative control} - \text{blank}} \times 100.$$

The cytotoxicity of each compound was expressed as half maximal cytotoxic concentration (CC_{50} values) against Hs27 cells. These values were calculated by a non-linear regression using GraphPad PRISM™ statistics software package (Version 9.5.1; San Diego, CA, U.S.A.) plotting the percentage viability against the log of compound concentrations.

Data Availability

All supporting data are included within the main article and its supplementary files. We uploaded the SAXS data to the Small Angle Scattering Biological Data Bank (SASBDB) [85], with the accession codes SASDS47. The structure of *Tg*DXR has been deposited in the Protein Databank (PDB) under accession code: 8S65.

Competing Interests

The authors declare that there are no competing interests associated with the manuscript.

PORTLAND PRESS

CRediT Author Contribution

Klaus Pfeffer: Conceptualization, Resources, Supervision, Funding acquisition, Project administration, Writing — review & editing. **Flaminia Mazzone**: Conceptualization, Data curation, Formal analysis, Validation, Investigation, Visualization, Methodology, Writing — original draft, Writing — review & editing. **Astrid Hoeppner**: Resources, Data curation, Formal analysis, Validation, Investigation, Visualization, Methodology, Writing — original draft, Writing — review & editing. **Jens Reiners**: Resources, Data curation, Formal analysis, Validation, Investigation, Visualization, Methodology, Writing — original draft, Writing — review & editing. **Christoph G.W. Gertzen**: Software, Formal analysis, Investigation, Visualization, Methodology, Writing — original draft, Writing — review & editing. **Violetta Applegate**: Data curation, Formal analysis, Validation, Investigation, Methodology, Writing — review & editing. **Mona Abdullah Abdullaziz**: Resources, Writing — review & editing. **Julia Gottstein**: Methodology, Writing — review & editing. **Daniel Degrandi**: Conceptualization, Supervision, Writing — review & editing. **Martina Wesemann**: Conceptualization, Methodology, Writing — review & editing. **Thomas Kurz**: Conceptualization, Resources, Supervision, Funding acquisition, Project administration, Writing — review & editing. **Sander H.J. Smits**: Conceptualization, Resources, Data curation, Formal analysis, Supervision, Funding acquisition, Investigation, Visualization, Writing — original draft, Project administration, Writing — review & editing.

Abbreviations

BSA, bovine serum albumin; DMSO, dimethyl sulfoxide; DXP, 1-Deoxy-D-xylulose 5-phosphate; EOM, Ensemble Optimisation Method; FBS, fetal bovine serum; IMDM, Iscove's Modified Dulbecco's medium; IPTG, *i*sopropyl-β-D-thiogalactopyranosid; LB, Luria-Bertani; MEP, 2-*C*-methyl-D-erythritol 4-phosphate; PCR, polymerase chain reaction; SAXS, small-angle X-ray scattering; SEC, size exclusion chromatography.

References

1 Levine, N.D. (2018) *The Protozoan Phylum Apicomplexa: Volume 2*, CRC Press, Boca Raton, FL
2 Lourido, S. (2019) *Toxoplasma gondii. Trends Parasitol.* **35**, 944–945 https://doi.org/10.1016/j.pt.2019.07.001
3 White, M.W. and Suvorova, E.S. (2018) Apicomplexa cell cycles: something old, borrowed, lost, and new. *Trends Parasitol.* **34**, 759–771 https://doi.org/10.1016/j.pt.2018.07.006
4 Centers for Disease Control and Prevention. Parasites - toxoplasmosis (toxoplasma infection) - epidemiology & risk factors, https://www.cdc.gov/parasites/toxoplasmosis/epi.html
5 Pleyer, U., Gross, U., Schlüter, D., Wilking, H. and Seeber, F. (2019) Toxoplasmosis in Germany: epidemiology, diagnosis, risk factors, and treatment. *Dtsch. Ärztebl. Int.* **116**, 435 https://doi.org/10.3238/arztebl.2019.0435
6 Krueger, W.S., Hilborn, E.D., Converse, R.R. and Wade, T.J. (2014) Drinking water source and human *Toxoplasma gondii* infection in the United States: a cross-sectional analysis of NHANES data. *BMC Public Health* **14**, 711 https://doi.org/10.1186/1471-2458-14-711
7 Montoya, J.G. and Liesenfeld, O. (2004) Toxoplasmosis. *Lancet* **363**, 1965–1976 https://doi.org/10.1016/S0140-6736(04)16412-X
8 Johnson, L.L. (1992) SCID mouse models of acute and relapsing chronic *Toxoplasma gondii* infections. *Infect Immun.* **60**, 3719–3724 https://doi.org/10.1128/iai.60.9.3719-3724.1992
9 Basavaraju, A. (2016) Toxoplasmosis in HIV infection: an overview. *Trop. Parasitol.* **6**, 129–135 https://doi.org/10.4103/2229-5070.190817
10 Deganich, M., Boudreaux, C. and Benmerzouga, I. (2022) Toxoplasmosis infection during pregnancy. *Trop. Med. Infect. Dis.* **8**, 3 https://doi.org/10.3390/tropicalmed8010003
11 Dunay, I.R., Gajurel, K., Dhakal, R., Liesenfeld, O. and Montoya, J.G. (2018) Treatment of toxoplasmosis: historical perspective, animal models, and current clinical practice. *Clin. Microbiol. Rev.* **31**(4), e00057-17 https://doi.org/10.1128/CMR.00057-17
12 Hemphill, A. and Müller, J. (2023) Toxoplasma gondii infection: novel emerging therapeutic targets. *Expert Opin. Ther. Targets* **27**, 293–304 https://doi.org/10.1080/14728222.2023.2217353
13 Alday, P.H. and Doggett, J.S. (2017) Drugs in development for toxoplasmosis: advances, challenges, and current status. *Drug Des. Devel. Ther.* **11**, 273–293 https://doi.org/10.2147/dddt.S60973
14 McFadden, G.I. (2011) The apicoplast. *Protoplasma* **248**, 641–650 https://doi.org/10.1007/s00709-010-0250-5

15   Hajj, R.E., Tawk, L., Itani, S., Hamie, M., Ezzeddine, J., El Sabban, M. et al. (2021) Toxoplasmosis: current and emerging parasite druggable targets. *Microorganisms* **9**, 2531 https://doi.org/10.3390/microorganisms9122531

16   Lim, L. and McFadden, G.I. (2010) The evolution, metabolism and functions of the apicoplast. *Phil. Trans. R. Soc. B* **365**, 749–763 https://doi.org/10.1098/rstb.2009.0273

17   Wang, X. and Dowd, C.S. (2018) The methylerythritol phosphate pathway: promising drug targets in the fight against tuberculosis. *ACS Infect. Dis.* **4**, 278–290 https://doi.org/10.1021/acsinfecdis.7b00176

18   Ball, H.S., Girma, M.B., Zainab, M., Soojhawon, I., Couch, R.D. and Noble, S.M. (2021) Characterization and inhibition of 1-deoxy-ᴅ-xylulose 5-phosphate reductoisomerase: a promising drug target in *Acinetobacter baumannii* and *Klebsiella pneumoniae. ACS Infect. Dis.* **7**, 2987–2998 https://doi.org/10.1021/acsinfecdis.1c00132

19   Allamand, A., Piechowiak, T., Lièvremont, D., Rohmer, M. and Grosdemange-Billiard, C. (2023) The multifaceted MEP pathway: towards new therapeutic perspectives. *Molecules* **28**, 1403 https://doi.org/10.3390/molecules28031403

20   Xu, M., Zhu, J., Diao, Y., Zhou, H., Ren, X., Sun, D. et al. (2013) Novel selective and potent inhibitors of malaria parasite dihydroorotate dehydrogenase: discovery and optimization of dihydrothiophenone derivatives. *J. Med. Chem.* **56**, 7911–7924 https://doi.org/10.1021/jm400938g

21   Proteau, P.J. (2004) 1-Deoxy-ᴅ-xylulose 5-phosphate reductoisomerase: an overview. *Bioorg. Chem.* **32**, 483–493 https://doi.org/10.1016/j.bioorg.2004.08.004

22   Singh, N., Chevé, G., Avery, M.A. and McCurdy, C.R. (2007) Targeting the methyl erythritol phosphate (MEP) pathway for novel antimalarial, antibacterial and herbicidal drug discovery: inhibition of 1-deoxy-D-xylulose-5-phosphate reductoisomerase (DXR) enzyme. *Curr. Pharm. Des.* **13**, 1161–1177 https://doi.org/10.2174/138161207780618939

23   Mac Sweeney, A., Lange, R., Fernandes, R.P., Schulz, H., Dale, G.E., Douangamath, A. et al. (2005) The crystal structure of *E. coli* 1-deoxy-D-xylulose-5-phosphate reductoisomerase in a ternary complex with the antimalarial compound fosmidomycin and NADPH reveals a tight-binding closed enzyme conformation. *J. Mol. Biol.* **345**, 115–127 https://doi.org/10.1016/j.jmb.2004.10.030

24   Andaloussi, M., Henriksson, L.M., Więckowska, A., Lindh, M., Björkelid, C., Larsson, A.M. et al. (2011) Design, synthesis, and X-ray crystallographic studies of α-aryl substituted fosmidomycin analogues as inhibitors of *Mycobacterium tuberculosis* 1-deoxy-ᴅ-xylulose 5-phosphate reductoisomerase. *J. Med. Chem.* **54**, 4964–4976 https://doi.org/10.1021/jm2000085

25   Umeda, T., Tanaka, N., Kusakabe, Y., Nakanishi, M., Kitade, Y. and Nakamura, K.T. (2011) Molecular basis of fosmidomycin's action on the human malaria parasite *Plasmodium falciparum. Sci. Rep.* **1**, 9 https://doi.org/10.1038/srep00009

26   Okuhara M, K.Y., Goto, T., Okamoto, M., Terano, H., Kohsaka, M., Aoki, H. et al. (1980) Studies on new phosphonic acid antibiotics III. isolation and characterization of FR-31564. *J. Antibiot.* **33**, 24–28 https://doi.org/10.7164/antibiotics.33.24

27   Kuzuyama, T., Shimizu, T., Takahashi, S. and Seto, H. (1998) Fosmidomycin, a specific inhibitor of 1-deoxy-D-xylulose 5-phosphate reductoisomerase in the nonmevalonate pathway for terpenoid biosynthesis. *Tetrahedron Lett.* **39**, 7913–7916 https://doi.org/10.1016/S0040-4039(98)01755-9

28   Jomaa, H., Wiesner, J., Sanderbrand, S., Altincicek, B., Weidemeyer, C., Hintz, M. et al. (1999) Inhibitors of the nonmevalonate pathway of isoprenoid biosynthesis as antimalarial drugs. *Science* **285**, 1573–1576 https://doi.org/10.1126/science.285.5433.1573

29   Na-Bangchang, K., Ruengweerayut, R., Karbwang, J., Chauemung, A. and Hutchinson, D. (2007) Pharmacokinetics and pharmacodynamics of fosmidomycin monotherapy and combination therapy with clindamycin in the treatment of multidrug resistant falciparum malaria. *Malar. J.* **6**, 70 https://doi.org/10.1186/1475-2875-6-70

30   Kuemmerle, H., Murakawa, T., Sakamoto, H., Sato, N., Konishi, T. and De Santis, F. (1985) Fosmidomycin, a new phosphonic acid antibiotic. Part II: 1. Human pharmacokinetics. 2. Preliminary early phase IIa clinical studies. *Int. J. Clin. Pharmacol. Ther. Toxicol.* **23**, 521–528

31   Sakamoto, Y., Furukawa, S., Ogihara, H. and Yamasaki, M. (2003) Fosmidomycin resistance in adenylate cyclase deficient (cya) mutants of *Escherichia coli. Biosci. Biotechnol. Biochem.* **67**, 2030–2033 https://doi.org/10.1271/bbb.67.2030

32   Brown, A.C. and Parish, T. (2008) Dxr is essential in *Mycobacterium tuberculosis* and fosmidomycin resistance is due to a lack of uptake. *BMC Microbiol.* **8**, 78 https://doi.org/10.1186/1471-2180-8-78

33   Nair, S.C., Brooks, C.F., Goodman, C.D., Strurm, A., McFadden, G.I., Sundriyal, S. et al. (2011) Apicoplast isoprenoid precursor synthesis and the molecular basis of fosmidomycin resistance in *Toxoplasma gondii. J. Exp. Med.* **208**, 1547–1559 https://doi.org/10.1084/jem.20110039

34   Kunfermann, A., Lienau, C., Illarionov, B., Held, J., Gräwert, T., Behrendt, C.T. et al. (2013) IspC as target for antiinfective drug discovery: synthesis, enantiomeric separation, and structural biology of fosmidomycin thia isosters. *J. Med. Chem.* **56**, 8151–8162 https://doi.org/10.1021/jm4012559

35   Lienau, C., Gräwert, T., Avelar, L.A.A., Illarionov, B., Held, J., Knaab, T.C. et al. (2019) Novel reverse thia-analogs of fosmidomycin: synthesis and antiplasmodial activity. *Eur. J. Med. Chem.* **181**, 111555 https://doi.org/10.1016/j.ejmech.2019.07.058

36   Brücher, K., Illarionov, B., Held, J., Tschan, S., Kunfermann, A., Pein, M.K. et al. (2012) α-Substituted β-oxa isosteres of fosmidomycin: synthesis and biological evaluation. *J. Med. Chem.* **55**, 6566–6575 https://doi.org/10.1021/jm300652f

37   Cai, G., Deng, L., Xue, J., Moreno, S.N., Striepen, B. and Song, Y. (2013) Expression, characterization and inhibition of *Toxoplasma gondii* 1-deoxy-D-xylulose-5-phosphate reductoisomerase. *Bioorg. Med. Chem. Lett.* **23**, 2158–2161 https://doi.org/10.1016/j.bmcl.2013.01.097

38   Goble, J.L., Johnson, H., De Ridder, J., Stephens, L.L., Louw, A., Blatch, G.L. et al. (2013) The druggable antimalarial target PfDXR: overproduction strategies and kinetic characterization. *Protein Pept. Lett.* **20**, 115–124 https://doi.org/10.2174/092986613804725253

39   Dhiman, R.K., Schaeffer, M.L., Bailey, A.M., Testa, C.A., Scherman, H. and Crick, D.C. (2005) 1-Deoxy-ᴅ-xylulose 5-phosphate reductoisomerase (IspC) from *Mycobacterium tuberculosis*: towards understanding mycobacterial resistance to fosmidomycin. *J. Bacteriol.* **187**, 8395–8402 https://doi.org/10.1128/JB.187.24.8395-8402.2005

40   Reuter, K., Sanderbrand, S., Jomaa, H., Wiesner, J., Steinbrecher, I., Beck, E. et al. (2002) Crystal structure of 1-deoxy-D-xylulose-5-phosphate reductoisomerase, a crucial enzyme in the non-mevalonate pathway of isoprenoid biosynthesis. *J. Biol. Chem.* **277**, 5378–5384 https://doi.org/10.1074/jbc.M109500200

41   Henriksson, L.M., Unge, T., Carlsson, J., Aqvist, J., Mowbray, S.L. and Jones, T.A. (2007) Structures of *Mycobacterium tuberculosis* 1-deoxy-D-xylulose-5-phosphate reductoisomerase provide new insights into catalysis. *J. Biol. Chem.* **282**, 19905–19916 https://doi.org/10.1074/jbc.M701935200

42   Yajima, S., Hara, K., Iino, D., Sasaki, Y., Kuzuyama, T., Ohsawa, K. et al. (2007) Structure of 1-deoxy-D-xylulose 5-phosphate reductoisomerase in a quaternary complex with a magnesium ion, NADPH and the antimalarial drug fosmidomycin. *Acta Crystallogr. Sect. F Struct. Biol. Cryst. Commun.* **63**, 466–470 https://doi.org/10.1107/s1744309107024475

43   Kuzuyama, T., Takahashi, S., Takagi, M. and Seto, H. (2000) Characterization of 1-deoxy-D-xylulose 5-phosphate reductoisomerase, an enzyme involved in isopentenyl diphosphate biosynthesis, and identification of its catalytic amino acid residues. *J. Biol. Chem.* **275**, 19928–19932 https://doi.org/10.1074/jbc.M001820200

44   Baumeister, S., Wiesner, J., Reichenberg, A., Hintz, M., Bietz, S., Harb, O.S. et al. (2011) Fosmidomycin uptake into Plasmodium and Babesia-infected erythrocytes is facilitated by parasite-induced new permeability pathways. *PLoS One* **6**, e19334 https://doi.org/10.1371/journal.pone.0019334

45   Angel, S.O., Vanagas, L., Ruiz, D.M., Cristaldi, C., Saldarriaga Cartagena, A.M. and Sullivan, Jr, W.J. (2020) Emerging therapeutic targets against *Toxoplasma gondii*: update on DNA repair response inhibitors and genotoxic drugs. *Front. Cell. Infect. Microbiol.* **10**, 289 https://doi.org/10.3389/fcimb.2020.00289

46   Rodriguez-Concepcion, M. (2004) The MEP pathway: a new target for the development of herbicides, antibiotics and antimalarial drugs. *Curr. Pharm. Des.* **10**, 2391–2400 https://doi.org/10.2174/1381612043384006

47   Woo, Y.H., Fernandes, R.P. and Proteau, P.J. (2006) Evaluation of fosmidomycin analogs as inhibitors of the *Synechocystis* sp. PCC6803 1-deoxy-D-xylulose 5-phosphate reductoisomerase. *Bioorg. Med. Chem.* **14**, 2375–2385 https://doi.org/10.1016/j.bmc.2005.11.012

48   Behrendt, C.T., Kunfermann, A., Illarionova, V., Matheeussen, A., Pein, M.K., Gräwert, T. et al. (2011) Reverse fosmidomycin derivatives against the antimalarial drug target IspC (Dxr). *J. Med. Chem.* **54**, 6796–6802 https://doi.org/10.1021/jm200694q

49   Behrendt, C.T., Kunfermann, A., Illarionova, V., Matheeussen, A., Gräwert, T., Groll, M. et al. (2010) Synthesis and antiplasmodial activity of highly active reverse analogues of the antimalarial drug candidate fosmidomycin. *ChemMedChem* **5**, 1673–1676 https://doi.org/10.1002/cmdc.201000276

50   Knak, T., Abdullaziz, M.A., Höfmann, S., Alves Avelar, L.A., Klein, S., Martin, M. et al. (2022) Over 40 years of fosmidomycin drug research: a comprehensive review and future opportunities. *Pharmaceuticals* **15**, 1553 https://doi.org/10.3390/ph15121553

51   Cui, J., Yang, X., Yang, J., Jia, R., Feng, Y. and Shen, B. (2022) A coccidia-specific phosphate transporter is essential for the growth of *Toxoplasma gondii* parasites. *Microbiol. Spectr.* **10**, e0218622 https://doi.org/10.1128/spectrum.02186-22

52   Haemers, T., Wiesner, J., Poecke, S.V., Goeman, J., Henschker, D., Beck, E. et al. (2006) Synthesis of α-substituted fosmidomycin analogues as highly potent *Plasmodium falciparum* growth inhibitors. *Bioorg. Med. Chem. Lett.* **16**, 1888–1891 https://doi.org/10.1016/j.bmcl.2005.12.082

53   Madeira, F., Pearce, M., Tivey, A.R., Basutkar, P., Lee, J., Edbali, O. et al. (2022) Search and sequence analysis tools services from EMBL-EBI in 2022. *Nucleic Acids Res.* **50**, W276–W279 https://doi.org/10.1093/nar/gkac240

54   Waterhouse, A.M., Procter, J.B., Martin, D.M.A., Clamp, M. and Barton, G.J. (2009) Jalview version 2—a multiple sequence alignment editor and analysis workbench. *Bioinformatics* **25**, 1189–1191 https://doi.org/10.1093/bioinformatics/btp033

55   Carter, P. (1986) Site-directed mutagenesis. *Biochem. J.* **237**, 1 https://doi.org/10.1042/bj2370001

56   Lee, P.Y., Costumbrado, J., Hsu, C.Y. and Kim, Y.H. (2012) Agarose gel electrophoresis for the separation of DNA fragments. *J. Vis. Exp.* **62**, 3923 https://doi.org/10.3791/3923

57   Wilkins, M.R., Gasteiger, E., Bairoch, A., Sanchez, J.-C., Williams, K.L., Appel, R.D. et al. (1999) Protein identification and analysis tools in the ExPASy server. In *2-D Proteome Analysis Protocols* (Link, A.J., ed.), pp. 531–552, Humana Press, Totowa, NJ.

58   Kabsch, W. (2010) XDS. *Acta Crystallogr. D Biol. Crystallogr.* **66**, 125–132 https://doi.org/10.1107/s0907444909047337

59   Evans, P.R. and Murshudov, G.N. (2013) How good are my data and what is the resolution? *Acta Crystallogr. D Biol. Crystallogr.* **69**, 1204–1214 https://doi.org/10.1107/s0907444913000061

60   Winn, M.D., Ballard, C.C., Cowtan, K.D., Dodson, E.J., Emsley, P., Evans, P.R. et al. (2011) Overview of the CCP4 suite and current developments. *Acta Crystallogr. D Biol. Crystallogr.* **67**, 235–242 https://doi.org/10.1107/s0907444910045749

61   McCoy, A.J., Grosse-Kunstleve, R.W., Adams, P.D., Winn, M.D., Storoni, L.C. and Read, R.J. (2007) Phaser crystallographic software. *J. Appl. Crystallogr.* **40**, 658–674 https://doi.org/10.1107/s0021889807021206

62   Emsley, P. and Cowtan, K. (2004) Coot: model-building tools for molecular graphics. *Acta Crystallogr. D Biol. Crystallogr.* **60**, 2126–2132 https://doi.org/10.1107/s0907444904019158

63   Emsley, P., Lohkamp, B., Scott, W.G. and Cowtan, K. (2010) Features and development of Coot. *Acta Crystallogr. D Biol. Crystallogr.* **66**, 486–501 https://doi.org/10.1107/s0907444910007493

64   Liebschner, D., Afonine, P.V., Baker, M.L., Bunkóczi, G., Chen, V.B., Croll, T.I. et al. (2019) Macromolecular structure determination using X-rays, neutrons and electrons: recent developments in Phenix. *Acta Crystallogr. D Struct. Biol.* **75**, 861–877 https://doi.org/10.1107/s2059798319011471

65   Pernot, P., Theveneau, P., Giraud, T., Fernandes, R.N., Nurizzo, D., Spruce, D. et al. (2010) New beamline dedicated to solution scattering from biological macromolecules at the ESRF. *J. Phys.: Conf. Ser.* **247**, 012009 https://doi.org/10.1088/1742-6596/247/1/012009

66   Pernot, P., Round, A., Barrett, R., De Maria Antolinos, A., Gobbo, A., Gordon, E. et al. (2013) Upgraded ESRF BM29 beamline for SAXS on macromolecules in solution. *J. Synchrotron Radiat.* **20**, 660–664 https://doi.org/10.1107/S0909049513010431

67   Manalastas-Cantos, K., Konarev, P.V., Hajizadeh, N.R., Kikhney, A.G., Petoukhov, M.V., Molodenskiy, D.S. et al. (2021) ATSAS 3.0: expanded functionality and new tools for small-angle scattering data analysis. *J. Appl. Crystallogr.* **54**, 343–355 https://doi.org/10.1107/S1600576720013412

68   Panjkovich, A. and Svergun, D.I. (2018) CHROMIXS: automatic and interactive analysis of chromatography-coupled small angle X-ray scattering data. *Bioinformatics* **34**, 1944–1946 https://doi.org/10.1093/bioinformatics/btx846

69   Konarev, P.V., Volkov, V.V., Sokolova, A.V., Koch, M.H.J. and Svergun, D.I. (2003) PRIMUS: a Windows PC-based system for small-angle scattering data analysis. *J. Appl. Crystallogr.* **36**, 1277–1282 https://doi.org/10.1107/S0021889803012779

70   Guinier, A. (1939) Diffraction of X-rays of very small angles-application of ultramicroscopic phenomenon. *Ann. Phys.* **12**, 161 https://doi.org/10.1051/anphys/193911120161

71   Svergun, D.I. (1992) Determination of the regularization parameter in indirect-transform methods using perceptual criteria. *J. Appl. Crystallogr.* **25**, 495–503 https://doi.org/10.1107/S0021889892001663

72   Bernado, P., Mylonas, E., Petoukhov, M.V., Blackledge, M. and Svergun, D.I. (2007) Structural characterization of flexible proteins using small-angle X-ray scattering. *J. Am. Chem. Soc.* **129**, 5656–5664 https://doi.org/10.1021/ja069124n

73 Tria, G., Mertens, H.D., Kachala, M. and Svergun, D.I. (2015) Advanced ensemble modelling of flexible macromolecules using X-ray solution scattering. *IUCrJ* **2**, 207–217 https://doi.org/10.1107/S205225251500202X

74 Dittrich, J., Schmidt, D., Pfleger, C. and Gohlke, H. (2019) Converging a knowledge-based scoring function: DrugScore2018. *J. Chem. Inf. Model.* **59**, 509–521 https://doi.org/10.1021/acs.jcim.8b00582

75 Sotriffer, C.A., Gohlke, H. and Klebe, G. (2002) Docking into knowledge-based potential fields: a comparative evaluation of DrugScore. *J. Med. Chem.* **45**, 1967–1970 https://doi.org/10.1021/jm025507u

76 Goodsell, D.S., Morris, G.M. and Olson, A.J. (1996) Automated docking of flexible ligands: applications of AutoDock. *J. Mol. Recognit.* **9**, 1–5 https://doi.org/10.1002/(sici)1099-1352(199601)9:1<1::aid-jmr241>3.0.co;2-6

77 Schrödinger, L.D.W. (2020) PyMOL. http://www.pymol.org/pymol

78 Merkt, F.K., Mazzone, F., Sazzadeh, S.S., Bonda, L., Hinz, L.K., Gruber, I. et al. (2021) Fluorescent Indolo [3, 2-a] phenazines against *Toxoplasma gondii*: concise synthesis by gold-catalyzed cycloisomerization with 1, 2-silyl migration and ipso-iodination Suzuki sequence. *Chemistry* **27**, 9774–9781 https://doi.org/10.1002/chem.202101391

79 Mazzone, F., Simons, V.E., van Geelen, L., Frank, M., Mándi, A., Kurtán, T. et al. (2022) In vitro biological activity of natural products from the endophytic fungus *Paraboeremia selaginellae* against *Toxoplasma gondii*. *Antibiotics* **11**, 1176 https://doi.org/10.3390/antibiotics11091176

80 Klischan, M.K.T., Mazzone, F., Berning, L., Greb, J., Schlamkow, M., Haase, M. et al. (2023) Modular approach for the synthesis and bioactivity profiling of 8,8′-biflavones. *ACS Omega* **8**, 41816–41834 https://doi.org/10.1021/acsomega.3c06503

81 Pfefferkorn, E. and Pfefferkorn, L.C. (1977) Specific labeling of intracellular *Toxoplasma gondii* with uracil. *J. Protozool.* **24**, 449–453 https://doi.org/10.1111/j.1550-7408.1977.tb04774.x

82 Konstantinovic, N., Guegan, H., Stäjner, T., Belaz, S. and Robert-Gangneux, F. (2019) Treatment of toxoplasmosis: current options and future perspectives. *Food Waterborne Parasitol.* **15**, e00036 https://doi.org/10.1016/j.fawpar.2019.e00036

83 Mosmann, T. (1983) Rapid colorimetric assay for cellular growth and survival: application to proliferation and cytotoxicity assays. *J. Immunol. Methods* **65**, 55–63 https://doi.org/10.1016/0022-1759(83)90303-4

84 Belmokhtar, C.A., Hillion, J. and Ségal-Bendirdjian, E. (2001) Staurosporine induces apoptosis through both caspase-dependent and caspase-independent mechanisms. *Oncogene* **20**, 3354–3362 https://doi.org/10.1038/sj.onc.1204436

85 Kikhney, A.G., Borges, C.R., Molodenskiy, D.S., Jeffries, C.M. and Svergun, D.I. (2020) SASBDB: towards an automatically curated and validated repository for biological scattering data. *Protein Sci.* **29**, 66–75 https://doi.org/10.1002/pro.3731

86 Frank, A. and Groll, M. (2017) The methylerythritol phosphate pathway to isoprenoids. *Chem. Rev.* **117**, 5675–5703 https://doi.org/10.1021/acs.chemrev.6b00537

87 Munos, J.W., Pu, X., Mansoorabadi, S.O., Kim, H.J. and Liu, H.-. (2009) A secondary kinetic isotope effect study of the 1-deoxy-D-xylulose-5-phosphate reductoisomerase-catalyzed reaction: evidence for a retroaldol-aldol rearrangement. *J. Am. Chem. Soc.* **131**, 2048–2049 https://doi.org/10.1021/ja807987h

88 Murkin, A.S., Manning, K.A. and Kholodar, S.A. (2014) Mechanism and inhibition of 1-deoxy-d-xylulose-5-phosphate reductoisomerase. *Bioorg. Chem.* **57**, 171–185 https://doi.org/10.1016/j.bioorg.2014.06.001